Master thesis

Modeling of viscous drops on soft substrates

Modellierung viskoser Tropfen auf weichen Substraten

Johannes Maximilian Kemper

Westfälische Wilhelms-Universität Münster
Institut für theoretische Physik

Supervisor: Prof. Dr. Uwe Thiele
Co-Supervisor: Dr. Svetlana Gurevich

This document is a slightly corrected version of the thesis submitted on 22.09.2015.

Abstract

The aim of this master thesis is to give a general model for liquid drops and films on soft substrates on the basis of the thin film equation. This topic has many applications in nature and technology. At first, a general viscoelastic model is described and then a simple elastic case is constructed that reproduces all physical phenomena that are expected like the formation of a ridge at the contact line. This simple elastic model is then continued with the library *auto07p* and is also set in cylindrical symmetry to account for the axisymmetric shape of unperturbed drops. From this a validity range of the elastic long-wave model is found to motivate time simulations. Finally, the time dependent model is simulated with finite element methods in the toolbox *Dune*.

Erklärung

Hiermit versichere ich, dass ich die vorliegende Arbeit mit dem Titel

Modellierung viskoser Tropfen auf weichen Substraten

selbständig verfasst habe, und dass ich keine anderen Quellen und Hilfsmittel als die angegebenen benutzt habe und dass die Stellen der Arbeit, die anderen Werken - auch elektronischen Medien - dem Wortlaut oder Sinn nach entnommen wurden, auf jeden Fall unter Angabe der Quelle als Entlehnung kenntlich gemacht worden sind.

Ort, Datum

Unterschrift

Contents

1 Introduction

In this work a general model for liquid drops and films on soft substrates is given. The setting of the model includes hydrodynamics, elasticity theory and statistical physics that have to be interwoven to form a comprehensive theory. Since the substrate on which the liquid film evolves is soft, it is useful to first define soft matter. In general, a soft material can be easily deformed at room temperature by external forces, e.g. thermal, gravitational or pressure forces [44]. A few examples of the various materials called soft matter are organic materials, complex fluids, foams, granular materials, liquid crystals, polymers and many more [41]. The films considered in this model have

Figure 1: Picture of a drop sitting on a leaf by Frank Goos. One can easily see that the contact angle exceeds 90°, so the liquid is non-wetting on this leaf.

a thickness from nanometers up to micrometers and therefore it is small compared to their areal expansion, these are called thin films. It is generally accepted in the community that such liquid films and drops are best described by thin film models. As is shown in the next section, the thin film equation is a continuity equation historically derived from the famous *Navier-Stokes* equation using the lubrication approximation first introduced by Reynolds [36]. Deviating from this, a modern derivation using minimal surfaces and the *Helmholtz* free energy functional is given and the afore mentioned derivation is shown only for the radial case. There are many different ongoing studies about thin films on subjects as coarsening [17] on structured substrates [45], evaporation [42] and dip-coating [16, 49] in applied mathematics as well as theoretical physics. Thin films are generally assumed to rest on a hard surface without explicitly mentioning it. In contrast to that, this work introduces a soft substrate on which the liquid film stays, therefore there are deformations of the substrate triggered by the presence of the liquid sitting on it. In detail, the feedback of a liquid

drop on the soft substrate at the contact line of the drop is given by capillary forces that drag the substrate up [27, 37] and therefore forms a ridge [48], while the *Laplace* pressure inside the drop pushes it down. The model developed in this work has applications in many different areas such as medicine (balance organ of the inner ear, tear film on the eye) [3, 40], material science (paint/liquid on rubber) [13], cosmetics (wet hair) [37] and many more. On top of that, it is interesting from a physical and mathematical point of view, because a stick-slip and therefore discontinuous motion of the contact line for a moving droplet can occur [21]. For low velocities the liquid contact line drags a soft matter ridge with it, whereas for very high velocities the ridge flows without reaching its full, stationary form. The stick-slip motion of the contact line of moving drops is only produced for a

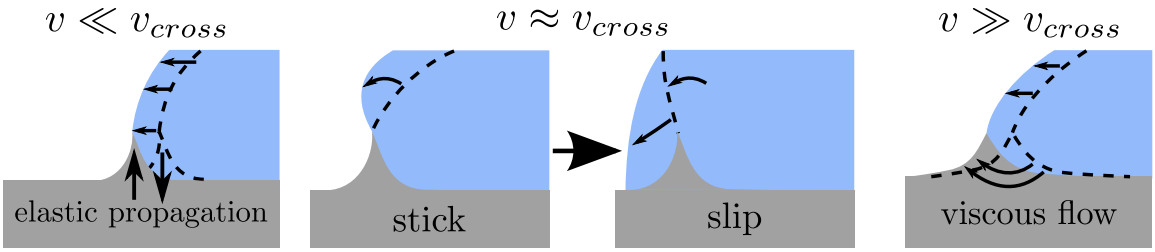

Figure 2: Sketch of the possible motions of a drop on a soft substrate according to [21].

specific cross velocity v_{cross} and is given by an interchange of pinning at the forming contact line and jumping over it as the contact angle increases over the critical angle. A similar phenomenon can also be found for receding contact lines [20].

Overall, this work is structured in two parts. The first introduces the theoretical details of the model and the second presents the results of simulations produced with *auto07p* and *DUNE* [10, 2].

2 Thin films

A thin film in the context of this work is a liquid layer whose thickness is small compared to its areal extend. This fact can be used to make an approximation to simplify the dynamics of the free boundary at the liquid-gas interface that is difficult to tread exactly.

2.1 Films and drops

The dominant effects that drive thin fluid films are surface tension and interactions with the substrate [17]. Of great significance for the behavior of films is the liquid-gas interface which in common parlance is called surface. The derivation starts from the usual continuity equation that, for the conservation of the film height h, reads:

$$\frac{\partial}{\partial t}h = -\nabla \cdot \mathbf{J}^{\mathrm{conv}}(h). \tag{2.1}$$

Here, $\mathbf{J}^{\mathrm{conv}}(h)$ is the convective flow of the liquid that can be expressed as the gradient of the pressure p of the liquid:

$$\mathbf{J}^{\mathrm{conv}}(h) = -\nabla p(h). \tag{2.2}$$

This is comparable to the flow in *Fick*'s first diffusion law, in which a concentration gradient drives the flow and from which the now commonly known diffusion equation is derived [15]. In nature, systems that are not continuously driven by external forces tend to minimize their free energy. This minimization of energy in the liquid film leads to the minimization of surface area because molecules at the surface have a higher binding energy than the molecules in the bulk [8]. This is due to the fact that the molecules have fewer interaction partners, which results in larger bounding lengths that take larger energies to hold. The liquid considered is incompressible $\nabla \cdot \mathbf{v} = 0$, in which $\mathbf{v} = 0$ is the flow velocity. The *Laplace* pressure for a spherical shape (drop), that is formed because surface area is minimized, is given by:

$$p_L = 2\gamma H. \tag{2.3}$$

This equation is known as the *Laplace* equation, in which $H = \frac{1}{2}(k_1 + k_2)$ is the mean curvature with the principal curvatures $k_{1,\max.}$ and $k_{2,\min.}$, both are $\frac{1}{r}$ for a 3D sphere, and γ is the surface tension. To describe more general forms of liquid surfaces we apply the theory of minimal surfaces that gives us a functional S that has to be minimized to get the surface, it reads:

$$S = \int_\Omega \mathrm{d}s = \int_\Omega \sqrt{|g_{ij}|}\,\mathrm{d}x = \int_\Omega \sqrt{|\mathbf{u}_{,i}^T \mathbf{u}_{,j}|}\,\mathrm{d}x. \tag{2.4}$$

The comma subscript denotes the derivative of the parametrization $\mathbf{u}$ with respect to the elements of the set of independent base coordinates $i, j \in \{x, y\}$ for a 2D model. Ω is the system domain

and the absolute value of the metric tensor $|g|$ means that its determinant has to be used. The parametrization $\mathbf{u}$ for a 2D model with the film thickness $h(x, y)$ is given by:

$$\mathbf{u} = \begin{pmatrix} x \\ y \\ h(x,y) \end{pmatrix}. \tag{2.5}$$

According to the equation (2.4) the metric tensor is:

$$(g_{ij}) = \begin{pmatrix} 1 + (\partial_x h)^2 & \partial_x h \partial_y h \\ \partial_x h \partial_y h & 1 + (\partial_y h)^2 \end{pmatrix} \tag{2.6}$$

and its determinant is given by:

$$\mathrm{Det}(g_{ij}) = 1 + (\partial_x h)^2 + (\partial_y h)^2 = 1 + (\nabla h)^2. \tag{2.7}$$

Therefore, the minimal surface functional is expressed as:

$$S = \int_\Omega \sqrt{1 + (\nabla h)^2}\, \mathrm{d}x. \tag{2.8}$$

With the surface tension γ as a proportionality constant this can be reinterpreted as the *Helmholz* free energy $\mathcal{F}_S$ of the surface:

$$\mathcal{F}_S = \int_\Omega \gamma \sqrt{1 + (\nabla h)^2}\, \mathrm{d}x. \tag{2.9}$$

Now, consider only systems in which the inclination is small $\nabla h \ll 1$, so we can do a *Taylor* expansion of the square root:

$$\mathcal{F}_S = \gamma A + \int_\Omega \frac{\gamma}{2} (\nabla h)^2\, \mathrm{d}x - \int_\Omega \frac{\gamma}{8} (\nabla h)^4\, \mathrm{d}x + \mathcal{O}((\nabla h)^6). \tag{2.10}$$

The first constant term is given by the definition of the surface tension $\gamma = \frac{\delta \mathcal{F}}{\delta A}$ [8]. Continuing the derivation of the thin film equation, we use only the second term of the series because the first term does not contribute to the form of the function to variate (its just a constant) and the higher order terms are increasingly smaller and thus neglected. Because of the square in $(\nabla h)^2$ and the positiveness of the surface tension γ, the second term is a strictly convex function, therefore a minimizer can be found for this functional. The pressure is defined by the variation of the free energy with respect to the surface function $p(h) = \frac{\delta \mathcal{F}[h]}{\delta h}$. The thin film equation accounting for capillarity and wettability for the film thickness $h(x, y, t)$ then reads:

$$\frac{\partial}{\partial t} h = -\nabla \cdot \mathbf{J}^{\mathrm{conv}}(h) = \nabla \cdot \left[Q(h) \nabla \frac{\delta \mathcal{F}[h]}{\delta h} \right]. \tag{2.11}$$

The mobility $Q(h)$ can be compared to *Ficks* diffusion constant [15] and describes how fluid the liquid is as a function of its thickness. For a *Poiseuille* flow in the film, that is characterized by being more fluid further away from the substrate, and no-slip boundary conditions at the substrate the mobility is given by $Q(h) = \frac{h^3}{3\eta}$, with the viscosity constant η. In equation (2.11) $\mathcal{F}[h]$ is the *Helmholtz* free energy functional that is also a *Lyapunov* functional $\mathrm{d}_t\mathcal{F} \leq 0$ [29], it reads:

$$\mathcal{F}[h] = \int_\Omega \left[\frac{\gamma}{2}(\nabla h)^2 + f(h)\right] \mathrm{d}x. \tag{2.12}$$

Therefore, the thin film equation is a gradient dynamics formulation, meaning that without an external force the system always goes to a stable state. It follows, that the convective flow in the continuity equation is given by:

$$\mathbf{J}^{\mathrm{conv}}(h) = -Q(h)\left(\nabla\frac{\delta\mathcal{F}[h]}{\delta h}\right) = -Q(h)\nabla p(h) = -Q(h)\nabla[-\gamma\,\triangle h - \Pi(h)]. \tag{2.13}$$

Here, $\frac{\delta\mathcal{F}[h]}{\delta h}$ is the *Frechét* derivative or functional derivative that in this case minimizes the free energy of the liquid-gas interface h. It is again clear, that the flow is driven by the gradient of the pressure $p(h)$ [42]. Specifically, the *Laplace* term $\gamma\,\triangle h$ is the curvature pressure that describes the

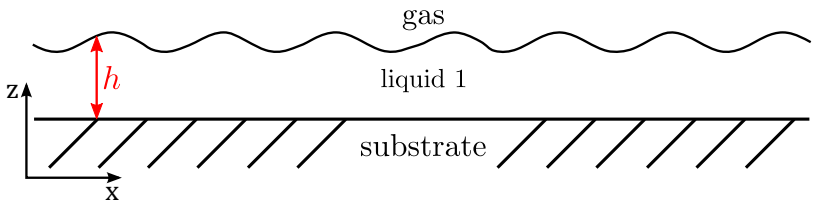

Figure 3: Sketch of the system described by the one layer thin film equation.

suppression of strong inclination, whereas $\Pi(h) = -\frac{\partial}{\partial h}f(h)$ is the disjoining pressure that introduces wettability effects and incorporates intermolecular forces, such as *Van der Waals* interactions and *Born* repulsion [33]. For more information see subsection (Disjoining pressure). For an alternative derivation of the thin film equation from the *Navier-Stokes* equation using lubrication approximation see subsection (2.2). As one can see, the conserved thin film equation is a nonlinear fourth-order parabolic equation [17] or, in physical terms, a *Cahn-Hillard* type equation. Because of this fourth-order differential operator the equation is hard to simulate numerically. Starting from a random initial field, one can see mass exchange that causes the emergence of drops from the film.

For the description of drops it is important to define the equilibrium contact angles between a liquid drop and a substrate. These depend on the surface tensions of the materials involved. To specify, the surface tension is the derivative of the free energy with respect to area and can here

be pictured as a force per unit length acting on the contact line. So, for example the solid-liquid surface tension γ_{sl} concerning a drop shape causes a radially inward force per unit length [19]. Combining this, the description of the forces acting on the contact line of a rigid substrate is given by the *Young-Laplace* condition that describes a force balance at the contact line (see figure 4):

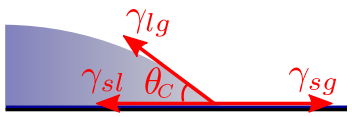

Figure 4: Sketch of the *Young* condition picturing the force balance at the contact line.

$$\gamma_{lg}\cos(\theta_C) = \gamma_{sg} - \gamma_{sl}. \tag{2.14}$$

Therefore, it is possible to predict the equilibrium contact angle θ_C knowing only the surface tensions of the materials involved. For example, if the surface tensions solid-gas γ_{sg} and solid-liquid γ_{sl} are the same, the equation gives an equilibrium contact angle of 90°. For viscoelastic substrates this relation changes to the *Neumann* condition that emerges naturally from the variation of the total free energy of this system [27]. The vertical component of the *Neumann* condition is then given by:

$$\gamma_{lg}\sin(\theta_C) = \gamma_{lg}\sin(\theta_l - \theta_{sl}) = \gamma_{sl}\sin(\theta_{sl}) + \gamma_{sg}\sin(\theta_{sg}) \tag{2.15}$$

and for the horizontal component follows similar to the *Young* condition (2.14):

$$\gamma_{lg}\cos(\theta_C) = \gamma_{lg}\cos(\theta_l - \theta_{sl}) = \gamma_{sg}\cos(\theta_{sg}) - \gamma_{sl}\cos(\theta_{sl}). \tag{2.16}$$

It should be clear from the figure (5) that the angles sum up to 2π. The three interface tensions form the sides of a triangle, if they satisfy the *Neumann* triangle inequalities [38]:

$$\gamma_{ij} < \gamma_{kj} + \gamma_{ki}, \text{ with } i,j,k \in \{l,s,g\}. \tag{2.17}$$

In the literature it is common to describe wetting with the spreading parameter S which is the

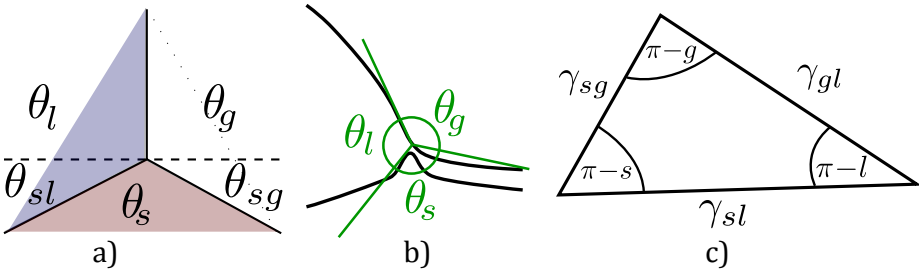

Figure 5: Sketches of the *Neumann* condition (a), angles (b) together with the *Neumann* triangle (c) in which s, l and g stand for the angles in their respective phases.

difference between the surface energy per unit area of the substrate when dry and wet: [8]

$$S = E_{S,\text{dry}} - E_{S,\text{wet}} = \gamma_{sg} - (\gamma_{sl} + \gamma_{lg}). \tag{2.18}$$

A liquid is called partially wetting, if the spreading parameter S is negative and totally wetting if it is positive. For partial wetting liquids a spherical cap resting on the substrate is formed, this is a drop with contact angle $\theta_C = \theta_{lg}$. Further, one differentiates between mostly wetting liquids $\theta_C \leq 90°$ and mostly non-wetting liquids $\theta_C > 90°$. Using the *Young* relation from above (2.14), one can also rewrite the spreading parameter S to:

$$S = \gamma_{lg} \cos(\theta_C - 1). \tag{2.19}$$

2.2 Derivation of the radial thin film equation

Starting from the incompressible *Navier-Stokes* equation, the thin film equation is derived in a radial form. There are different physical quantities in the equation, the liquid density ρ, the dynamic viscosity μ and the stream velocity u_i:

$$\rho \left[\frac{\partial u_i}{\partial t} + (u_j \nabla_j)\, u_i \right] = -(\nabla p)_i + \mu \triangle u_i + F_i, \tag{2.20}$$

moreover $F_i = -(\nabla \phi)_i$ is an external force given by the gradient of the potential ϕ. In addition, the incompressibility condition of the liquid applies $\nabla_i u_i = 0$. To obtain the radial form cylindrical coordinates are used, in which the linear differential operators are given by:

$$\nabla f = \frac{\partial f}{\partial r} \cdot \hat{e}_r + \frac{1}{r} \frac{\partial f}{\partial \varphi} \cdot \hat{e}_\varphi + \frac{\partial f}{\partial z} \cdot \hat{e}_z, \tag{2.21}$$

$$\nabla_i f_i = \frac{1}{r} \frac{\partial}{\partial r}(r f_r) + \frac{1}{r} \frac{\partial f_\varphi}{\partial \varphi} + \frac{\partial f_z}{\partial z}, \tag{2.22}$$

$$\triangle f = \frac{1}{r} \frac{\partial}{\partial r} \left(r \frac{\partial f}{\partial r} \right) + \frac{1}{r^2} \frac{\partial^2 f}{\partial \varphi^2} + \frac{\partial^2 f}{\partial z^2}. \tag{2.23}$$

Assuming rotational invariance the terms containing the polar angle φ are neglected. This results in the following two equations (devided by the density ρ) for the remaining components (r, z).

$$\text{r:}\ \frac{\partial u_r}{\partial t} + u_r \frac{\partial u_r}{\partial r} + u_z \frac{\partial u_r}{\partial z} = -\frac{1}{\rho} \frac{\partial p}{\partial r} + \nu \left(\frac{\partial^2 u_r}{\partial r^2} + \frac{1}{r} \frac{\partial u_r}{\partial r} + \frac{\partial^2 u_r}{\partial z^2} - \frac{u_r}{r^2} \right) - \frac{1}{\rho} \frac{\partial \phi}{\partial r}, \tag{2.24}$$

$$\text{z:}\ \frac{\partial u_z}{\partial t} + u_r \frac{\partial u_z}{\partial r} + u_z \frac{\partial u_z}{\partial z} = -\frac{1}{\rho} \frac{\partial p}{\partial z} + \nu \left(\frac{\partial^2 u_z}{\partial r^2} + \frac{1}{r} \frac{\partial u_z}{\partial r} + \frac{\partial^2 u_z}{\partial z^2} \right) - \frac{1}{\rho} \frac{\partial \phi}{\partial z}, \tag{2.25}$$

$$\text{inc. cond.:}\ \frac{1}{r} u_r + \frac{\partial u_r}{\partial r} + \frac{\partial u_z}{\partial z} = 0. \tag{2.26}$$

Therein, $\nu = \frac{\mu}{\rho}$ is the kinematic viscosity and incompressibility condition is shortened to inc. cond.. Due to the extremely differently sized extensions of the system in r-direction L and z-direction l, one can define the smallness parameter $\epsilon = \frac{l}{L}$. Now the following substitution rules are applied to make the equations dimensionless:

Table 1: Replacement rules for nondimensionalization of the radial *Navier-Stokes* equation.

t	r	z	$(\vec{\tau}_0,\epsilon\vec{\pi}_0),(\phi,p)$	Re,C	h,σ
$t=\frac{l}{\epsilon u_0}\,T$	$r=\frac{l}{\epsilon}\,R$	$z=l\,Z$	$(\vec{\tau}_0,\epsilon\vec{\pi}_0)=\frac{\mu u_0}{l}\,(\vec{\tau},\vec{\Pi})$	$\mathrm{Re}=\frac{u_0 l}{\nu}$	$h=l\,H$
$\frac{\partial}{\partial t}=\frac{\epsilon u_0}{l}\,\frac{\partial}{\partial T}$	$\frac{\partial}{\partial r}=\frac{\epsilon}{l}\,\frac{\partial}{\partial R}$	$\frac{\partial}{\partial z}=\frac{1}{l}\,\frac{\partial}{\partial Z}$	$(\phi,p)=\frac{\mu u_0}{\epsilon l}\,(\Phi,P)$	$\mathrm{C}=\frac{u_0\mu}{\sigma}$	$\sigma=\frac{\mu u_0}{\epsilon}\,\Sigma$
	$u_r=u_0\,u_R$	$u_z=\epsilon u_0\,u_Z$			

Thus, the resulting equations are (see appendix A for details):

$$\text{r: } \epsilon\mathrm{Re}\left(\frac{\partial u_R}{\partial T}+u_R\frac{\partial u_R}{\partial R}+u_Z\frac{\partial u_R}{\partial Z}\right)=-\frac{\partial P}{\partial R}+\frac{\partial^2 u_R}{\partial Z^2}+\epsilon^2\left(\frac{\partial^2 u_R}{\partial R^2}+\frac{1}{R}\frac{\partial u_R}{\partial R}-\frac{u_R}{R^2}\right)-\frac{\partial\Phi}{\partial R}, \quad (2.27)$$

$$\text{z: } \epsilon^3\mathrm{Re}\left(\frac{\partial u_Z}{\partial T}+u_R\frac{\partial u_Z}{\partial R}+\frac{\partial u_Z}{\partial Z}\right)=-\frac{\partial P}{\partial Z}+\epsilon^4\left(\frac{\partial^2 u_Z}{\partial R^2}+\frac{1}{R}\frac{\partial u_Z}{\partial R}\right)+\epsilon^2\frac{\partial^2 u_Z}{\partial Z^2}-\frac{\partial\Phi}{\partial Z}, \quad (2.28)$$

$$\text{inc. cond.: } \frac{1}{R}u_R+\frac{\partial u_R}{\partial R}+\frac{\partial u_Z}{\partial Z}=0. \quad (2.29)$$

The boundary conditions for the thin film equation are given in [32], at $Z=0$ this gives:

$$u_R-\beta_0\frac{\partial u_R}{\partial Z}=0, \qquad u_Z=0 \quad (2.30)$$

and for $Z=H(R,T)$ these are:

$$(\partial_Z u_R+\epsilon^2\partial_R u_Z)[1-\epsilon^2(\partial_R H)^2]-4\epsilon^2(\partial_R H)(\partial_R u_R)=\tau_0[1+\epsilon^2(\partial_R H)^2]+\partial_R\Sigma[1+\epsilon^2(\partial_R H)^2]^{1/2},$$

$$\frac{2\epsilon^2}{[1+\epsilon^2\,(\partial_R H)^2]}\{\partial_R u_R[\epsilon^2(\partial_R H)^2-1]-\partial_R H(\partial_Z u_R+\epsilon^2\partial_R u_Z)\}=\frac{C^{-1}\epsilon^3\partial_R^2 H}{[1+\epsilon^2(\partial_R H)^2]^{3/2}}+P+\Pi_0, \quad (2.31)$$

$$u_Z=\partial_T H+u_R\partial_R H.$$

One now integrates from 0 to $H(R,T)$ over the incompressibility condition in $\mathrm{d}Z$, in the process the last constraint from above is used:

$$\int_0^{H(R,T)}\frac{1}{R}u_R+\frac{\partial u_R}{\partial R}+\frac{\partial u_Z}{\partial Z}\mathrm{d}Z=0, \quad (2.32)$$

$$\frac{\partial H}{\partial T}+u_R\frac{\partial H}{\partial R}+\int_0^{H(R,T)}\frac{1}{R}u_R+\frac{\partial u_R}{\partial R}\mathrm{d}Z=0, \quad (2.33)$$

$$\frac{\partial H}{\partial T}+\frac{\partial}{\partial R}\left(\int_0^{H(R,T)}u_R\mathrm{d}Z\right)+\frac{1}{R}\left(\int_0^{H(R,T)}u_R\mathrm{d}Z\right)=0. \quad (2.34)$$

From the second to the third step the product rule of differential calculus is applied. Furthermore, in accordance with [32] the radial velocity u_R, after integrating the equations (2.27,2.28) up to order ϵ^0, is given by:

$$u_R = \left(\tau_0 + \frac{\partial \Sigma}{\partial R}\right)(Z + \beta_0) + \frac{\partial \overline{P}}{\partial R}\left(\frac{1}{2}Z^2 - HZ - \beta_0 H\right), \tag{2.35}$$

wherein $\overline{P} = P + \Phi$. This velocity is now incorporated in equation (2.34) and another integration is used:

$$\frac{\partial H}{\partial T} + \frac{1}{R}\frac{\partial}{\partial R}\left\{R\left[\left(\tau_0 + \frac{\partial \Sigma}{\partial R}\right)\left(\frac{1}{2}H^2 + \beta_0 H\right) - \frac{\partial \overline{P}}{\partial R}\left(\frac{1}{3}H^3 + \beta_0 H^2\right)\right]\right\} = 0. \tag{2.36}$$

If one now assumes $\tau_0 = \beta_0 = \Sigma = 0$ one gets the thin film equation in radial form:

$$\frac{\partial H}{\partial T} = \frac{1}{R}\frac{\partial}{\partial R}\left\{R\left[\frac{1}{3}H^3\frac{\partial \overline{P}}{\partial R} - \frac{1}{2}H^2\frac{\partial \Sigma}{\partial R}\right]\right\}. \tag{2.37}$$

This relatively long derivation can be spared, if one assumes that one knows the *Cartesian* thin film equation.

Starting from the thin film equation without *Marangoni* term, one can alternatively derive the full polar equation with φ dependence:

$$\frac{\partial h}{\partial t} = \nabla \cdot [Q(h)\nabla p] \tag{2.38}$$

$$= \nabla \cdot \left[Q(h)\left(\frac{\partial p}{\partial r} \cdot \vec{e}_r + \frac{1}{r}\frac{\partial p}{\partial \varphi} \cdot \vec{e}_\varphi\right)\right] \tag{2.39}$$

$$= \frac{1}{r}\frac{\partial}{\partial r}\left(rQ(h)\frac{\partial p}{\partial r}\right) + \frac{1}{r}\frac{\partial}{\partial \varphi}\left(\frac{Q(h)}{r}\frac{\partial p}{\partial \varphi}\right). \tag{2.40}$$

Wherein, $Q(h)$ is the mobility. When forming the equation, the cylindrical symmetric form of the gradient (2.21) and of the divergence (2.22) is used.

2.3 Disjoining pressure

When considering quantities like pressure or surface tension, one normally uses a macroscopic description of the system in focus. Since the films in our model are thin, we also have to consider microscopic interactions [8]. There are many different interaction forces between different fluids and different substrates that, in addition, vary with the thickness of the fluid considered. Therefore, we restrict our focus on one form of the interaction potential $f(h)$ from which the disjoining pressure follows by derivation:

$$\Pi(h) = -\frac{\partial}{\partial h} f(h). \tag{2.41}$$

For wetting and coarsening effects we need a long range attraction that is given by *Van-der-Waals* forces and a short range repulsion given by *Born* repulsion. One possible free energy function that

incorporates both these effects is given by:

$$f(h) = \frac{1}{2}\frac{1}{h^2}\left[1 - \frac{2}{5}\left(\frac{h_{pc}}{h}\right)^3\right]. \tag{2.42}$$

Here, h_{pc} is the precursor height that covers the whole substrate and is given by the unique minimum value of the free energy function (see figure (6)):

$$\Pi(h) = \frac{1}{h^3}\left[1 - \left(\frac{h_{pc}}{h}\right)^3\right]. \tag{2.43}$$

The precursor film is generally assumed to be thin compared to the liquid film in consideration, hence it has negligible macroscopic effects. For a more elaborate derivation of this disjoining pressure using nonlocal diffuse interface theory, see [33]. Both these functions may go to zero as their argument goes to infinity because the effects produced by the free energy function (potential) should not act on the liquid for large distances from the substrate, as these are short range effects [17].

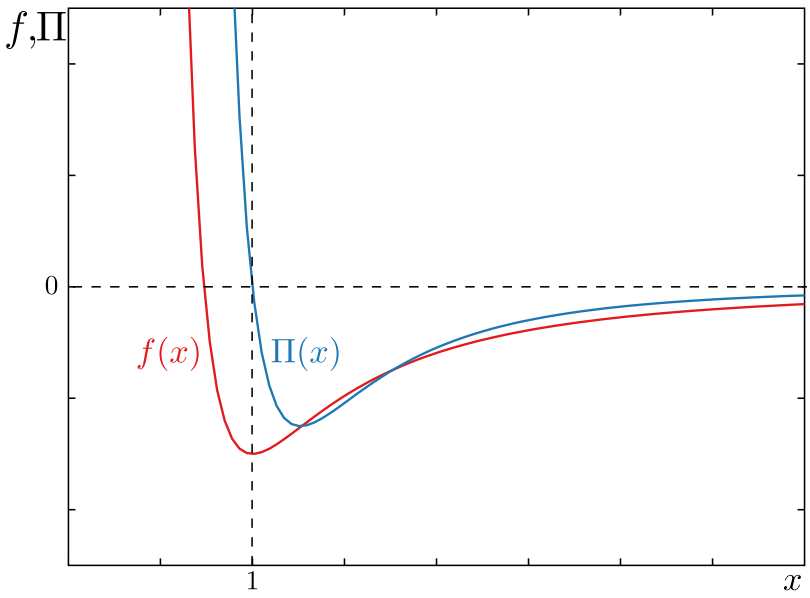

Figure 6: Plot of the free energy function $f(x)$ and the associated disjoining pressure $\Pi(x) = -\partial_x f(x)$.

Using the *Young* condition (2.14) and the fact that the disjoining free energy function is comparable

to the wetting energy, one gets:

$$\gamma_{sg} - \gamma_{sl} = \gamma_{lg} + f(h_{pc}), \tag{2.44}$$

$$\gamma_{lg}\cos(\theta_E) = \gamma_{lg} + \frac{1}{2h_{pc}^2} - \frac{h_{pc}^3}{5h_{pc}^5}, \tag{2.45}$$

$$h_{pc}^2\gamma_{lg}(\cos(\theta_E) - 1) = \frac{3}{10}. \tag{2.46}$$

The equilibrium angle $\theta_E = \epsilon\theta_{lg} = \frac{h_{pc}}{L}\theta_{lg}$ is small $\theta_E \ll 1$, so a *Taylor* series for the cosine can be performed.

$$\cos\left(\frac{h_{pc}}{L}\theta_{lg}\right) \approx 1 - \left(\frac{h_{pc}}{L}\right)^2 \frac{\theta_{lg}^2}{2} + \mathcal{O}(\theta_{lg}^4). \tag{2.47}$$

From the derivation of the thin film equation using lubrication approximation it follows that $L = h_{pc}^2\sqrt{\gamma_{lg}}$ and one gets:

$$\theta_{lg} = \sqrt{\frac{3}{5}} \approx 0.7746. \tag{2.48}$$

Throughout this work the precursor height of $h_{pc} = 1$ is used. All the models also are two coupled thin films with heights h and ξ that both can be deformed and this results in the arguments of the disjoining pressure $\Pi(h - \xi)$. One could argue that a geometric factor is needed to describe the distance of the interfaces $\|h - \xi\|$, but the factor looks like this:

$$\sqrt{1 + (\partial_x h(x))^2}\,\Pi(h) = \left(1 + \frac{1}{2}(\partial_x h(x))^2 + \mathcal{O}(h(x)^4)\right)\,\Pi(h). \tag{2.49}$$

In lubrication approximation the second term is of order ϵ^2 so it can be neglected and all higher order terms are even smaller so they can be dropped and just $\Pi(h)$ is left.

2.4 Two coupled thin film equations and mobility matrix

To couple thin film equations with the height of the upper layer h and lower layer height ξ, one has to combine the layers in one vector that reads:

$$\mathbf{\Psi} = \begin{pmatrix} h \\ \xi \end{pmatrix}, \tag{2.50}$$

with this, the multi layer thin film equation reads:

$$\frac{\partial}{\partial t}\Psi_i = \nabla \cdot [Q_{ij}(\nabla p(\Psi_j))] = \nabla \cdot \left[Q_{ij}\left(\nabla \frac{\delta \mathcal{F}}{\delta \Psi_j}\right)\right]. \tag{2.51}$$

Here, Q_{ij} is the mobility matrix, that is sometimes referred to as the inverse of the resistance matrix known from *Stokes*ian dynamics [5]. Showing again that the free energy is a *Lyapunov* functional

by multiplying the equation (2.51) from left with $\left(\nabla \frac{\delta \mathcal{F}}{\delta \Psi_i}\right)$, one gets [35]:

$$\frac{\mathrm{d}\mathcal{F}}{\mathrm{d}t} = -\int_\Omega \left(\nabla \frac{\delta \mathcal{F}}{\delta \Psi_i}\right) Q_{ij} \left(\nabla \frac{\delta \mathcal{F}}{\delta \Psi_j}\right) \mathrm{d}x = -\int_\Omega J_i \, Q_{ij} \, J_j \, \mathrm{d}x. \tag{2.52}$$

Since the mobility matrix is positive semi-definite, the free energy change $\frac{\mathrm{d}\mathcal{F}}{\mathrm{d}t}$ is always negative and thus the equation fulfills gradient dynamics. One example for a mobility matrix is:

$$Q_{ij} = \frac{1}{3\eta} \begin{pmatrix} h^3 & h^2\xi \\ h^2\xi & h\xi^2 + 3D\xi \end{pmatrix}, \tag{2.53}$$

where D is a diffusion constant [43]. All interactions between the layers and the subsoil are again contained in the form of the free energy potential $f(\Psi)$ that, after the functional derivative, gives a disjoining pressure of $\Pi_{h,\xi} = -\partial_{h,\xi} f(h,\xi)$. This matrix has to be symmetric, $Q_{ij} = Q_{ji}$, because of the second law of thermodynamics and especially microscopic reversibility, as is shown in the next subsection.

2.5 *Onsager*s variational principle and *Zwanzig*s generalization

In the context of coupled thin film equations, the mobility is given by a positive semi definite matrix that satisfies the reciprocal relation:

$$Q_{ij} = Q_{ji}. \tag{2.54}$$

This follows directly from *Onsager*'s variational principle, therefore a short summary of the theory is given here. In the context of this work, it is also interesting to include memory effects that are known to occur in relaxation processes. Because *Onsager*s theory only applies to systems in which the response of the system is simultaneous with the application of an external force, a generalization by *Zwanzig* is presented to include such relaxation effects. [51]

To start, a closed system that is slightly out of equilibrium with a defined entropy maximum $\mathcal{S}_{\max}$, which is always reached by relaxation and corresponds to its equilibrium state $\mathcal{S}_E = \mathcal{S}_{\max}$, is needed. There is now a set of coarse grained variables α_i with $i \in \{1, \ldots, n\}$ which themselves represent the degree of non-equilibrium of the system, meaning they are defined relative to their equilibrium values $\alpha_{i,E}$. A further assumption is that these variables give a complete description of the approach to equilibrium, so they all have non-equilibrium values different from their equilibrium values. The easiest form of the rate of change of these variables has to be a linear sum of the form:

$$\dot{\alpha}_i = -\lambda_{ik} \alpha_k, \tag{2.55}$$

in which the coefficient matrix λ_{ik} is constant in time. In such a system with fluctuations the entropy $\mathcal{S}(x_1, \ldots, x_n)$ expanded in powers of x_i till second order minus the equilibrium entropy $\mathcal{S}_E$ reads [24]:

$$\Delta\mathcal{S} = \mathcal{S} - \mathcal{S}_E = -\frac{1}{2}\beta_{ik}\alpha_i\alpha_k. \tag{2.56}$$

The thermodynamic force $\mathcal{X}$ conjugate to the thermodynamic quantities α_i is given by a superposition of them:

$$\mathcal{X}_i = -\frac{\partial\Delta\mathcal{S}}{\partial\alpha_i} = \beta_{ik}\alpha_k. \tag{2.57}$$

Because it follows from a second derivative of the entropy, the matrix β_{ik} is symmetrical. Substituting equation (2.57) into equation (2.55) one gets the characteristic form of the time evolution equation for the irreversible state:

$$\frac{\mathrm{d}}{\mathrm{d}t}\alpha_i(t) = \left\{-\lambda\beta^{-1}\right\}_{ij}\mathcal{X}_j(t) = L_{ij}\mathcal{X}_j(t). \tag{2.58}$$

The matrices L_{ij} are the symmetrical $L_{ij} = L_{ji}$ and positive semi-definite transport coefficients [30]. The symmetrical condition follows from microscopic time reversibility. Taking the time average that is denoted by an overline [31], one gets:

$$\overline{\alpha_i(t)\alpha_j(t+\Delta t)} = \overline{\alpha_i(t+\Delta t)\alpha_j}. \tag{2.59}$$

If one now differentiates this equation with respect to Δt and then lets it go to zero in the result, it reads:

$$\overline{\alpha_i\dot{\alpha}_j} = \overline{\dot{\alpha}_i\alpha_j}. \tag{2.60}$$

Substitution of equation (2.58) into this result gives:

$$\overline{\alpha_i L_{kl}\mathcal{X}_l} = \overline{L_{il}\mathcal{X}_l\alpha_k}. \tag{2.61}$$

From statistical physics it is known that $\overline{\alpha_i\mathcal{X}_j} = \delta_{ij}$, wherein δ_{ij} is the *Kronecker* delta. [24] Therefore, it follows:

$$(L_{kl}\delta_{il} = L_{il}\delta_{lk}) \Leftrightarrow L_{ki} = L_{ik}. \tag{2.62}$$

To sum this up, the *Onsager* relation follows from time reversal symmetry and therefore from the inherent property of energy conservation of a closed system. Let us now show the connection to the mobility matrix of the thin film equation. In his original paper *Onsager* used a temperature dependent version of the principle of least energy dissipation. The systems in this work are all isothermal, thus it is sufficient to minimize the *Rayleighian* $\mathcal{R}$ of the system that can be derived from hydrodynamics considerations (see [11] for more details):

$$\mathcal{R} = \frac{1}{2}\zeta_{ij}\dot{\mathcal{X}}_i\dot{\mathcal{X}}_j + \frac{\delta\mathcal{F}}{\delta\mathcal{X}_i}\dot{\mathcal{X}}_i, \tag{2.63}$$

wherein $\mathcal{F}$ is the *Helmholtz* free energy specific to the slightly non-equilibrium system in focus. *Onsager*s variational principle, expressed as a kinetic equation, then reads [11]:

$$\frac{\mathrm{d}}{\mathrm{d}t}\mathcal{X}_i = -\left(\zeta^{-1}\right)_{ij}\frac{\delta\mathcal{F}}{\delta\mathcal{X}_j}. \tag{2.64}$$

As stated before, *Onsager*s theory requires the system to respond instantaneous to an applied force. In general, such a response comes after the application of the force, so another more general theory is needed. The general result produced by *Zwanzig* from microscopic statistical reflections using the *Mori-Zwanzig* projection operator is given by the convolution [51]:

$$\frac{\mathrm{d}}{\mathrm{d}t}\alpha_i = \int_0^t K_{ij}(s)\mathcal{X}_j(\alpha_1(t-s),\ldots,\alpha_n(t-s))\,\mathrm{d}s. \tag{2.65}$$

The memory functions $K_{ij}(s)$ are comparable to *Onsager*s reciprocity coefficients and are related to them by the integral:

$$L_{ij} = \int_0^\tau K_{ij}(s)\,\mathrm{d}s. \tag{2.66}$$

The upper time limit τ is a substantial time, but shorter than the time the system needs to return its initial state after applying a force, for a closed system this time is called *Poincaré* recurrence time. The memory function itself is then given by the specific material, see section (Basics of polymer models).

3 Theory of elasticity

Fundamental to the description of deformations of bodies is the displacement vector:

$$u_i = x_i' - x_i. \tag{3.1}$$

Prior to the displacement, the positions are given by the coordinate x_i. After a displacement on the initial state is applied the positions change, this is shown by the prime x_i'. Given a displacement vector the deformation of a body is fully described. The infinitesimal distance between two points before and after deformation (using sum convention) gives:

$$\mathrm{d}l^2 = \mathrm{d}x_i^2, \qquad \mathrm{d}l'^2 = \mathrm{d}x_i'^2 = (\mathrm{d}x_i + \mathrm{d}u_i)^2 = (\mathrm{d}x_i)^2 + 2\mathrm{d}x_i\mathrm{d}u_i + (\mathrm{d}u_i)^2. \tag{3.2}$$

Due to the total differential of the displacement vector it is now possible to substitute $\mathrm{d}u_i = \frac{\partial u_i}{\partial x_k}\,\mathrm{d}x_k$ and it follows:

$$\mathrm{d}l'^2 = \mathrm{d}l^2 + 2\frac{\partial u_i}{\partial x_k}\mathrm{d}x_i\mathrm{d}x_k + \frac{\partial u_i}{\partial x_k}\frac{\partial u_i}{\partial x_l}\mathrm{d}x_k\mathrm{d}x_l. \tag{3.3}$$

Moreover, we rewrite this expression by using the independence of the indices in the summation:

$$\begin{aligned}
\mathrm{d}l'^2 =& \mathrm{d}l^2 + \left(\frac{\partial u_i}{\partial x_k} + \frac{\partial u_k}{\partial x_i}\right)\mathrm{d}x_i\mathrm{d}x_k + \frac{\partial u_l}{\partial x_k}\frac{\partial u_l}{\partial x_i}\mathrm{d}x_k\mathrm{d}x_i, \\
=& \mathrm{d}l^2 + \left(\frac{\partial u_i}{\partial x_k} + \frac{\partial u_k}{\partial x_i} + \frac{\partial u_l}{\partial x_k}\frac{\partial u_l}{\partial x_i}\right)\mathrm{d}x_k\mathrm{d}x_i, \\
=& \mathrm{d}l^2 + \varepsilon_{ik}\,\mathrm{d}x_k\mathrm{d}x_i.
\end{aligned}$$

This short calculation gives us the symmetric tensor $\varepsilon_{ik} = \varepsilon_{ki}$ that is called strain tensor [25]. For small displacements $u_i \ll 1$ one can identify the third term in the strain tensor as a second order term, therefore the tensor is to first order given by:

$$\varepsilon_{ik} = \frac{\partial u_i}{\partial x_k} + \frac{\partial u_k}{\partial x_i}. \tag{3.4}$$

Focusing on the resulting forces, one recognizes that the sum of all forces acting on a volume element gives the resulting force. Since force has a vector character one can (without loss of generality) write it as a divergence of a second order tensor. Using *Gauss*' law, to transform a volume integral into a surface integral, one gets:

$$F_i^{\mathrm{res}} = \int F_i\,\mathrm{d}V = \int \frac{\partial \sigma_{ik}}{\partial x_k}\,\mathrm{d}V = \oint \sigma_{ik}\,\mathrm{d}a_k. \tag{3.5}$$

This second order tensor σ_{ik} is the stress tensor that is also symmetric. It describes a force that acts in the direction of $\hat{e}_k$ perpendicular to a surface that is defined by the normal vector $\hat{e}_i$. (see figure (7))

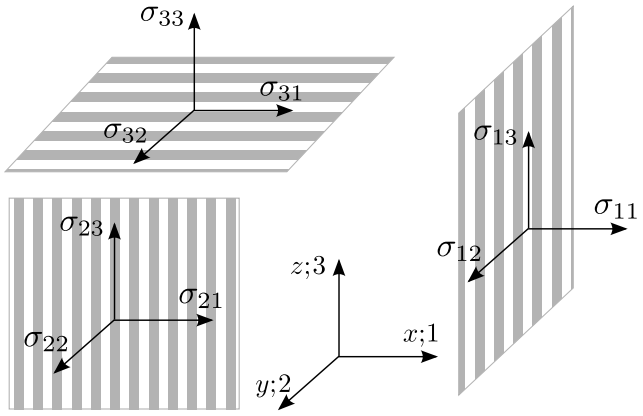

Figure 7: Sketch showing the components of the stress tensor [14].

The general form of the equation of motion for an elastic medium, with the density of the medium ρ is given by [25]:

$$\rho \ddot{u}_i = \nabla \cdot \underline{\underline{\sigma}} = \frac{\partial \sigma_{ij}}{\partial x_j}. \tag{3.6}$$

While for an isotropic medium with external forces it reads:

$$\rho \ddot{\mathbf{u}} = \frac{Y}{(1+\nu)} \operatorname{div} \operatorname{grad} \mathbf{u} + \frac{Y}{(1+\nu)(1-2\nu)} \operatorname{grad} \operatorname{div} \mathbf{u}, \tag{3.7}$$

where the gradient acting on a vector field is defined as a gradient applied to each component. The Young's modulus Y is the reciprocal of the coefficient of elasticity that is defined with the shear modulus μ and the compression modulus K by:

$$Y = \frac{9KG}{3K+G}, \qquad K = \lambda + \frac{2}{3}G. \tag{3.8}$$

λ and G are also called the first and second *Lamé* coefficients. Often, the *Poisson* ratio ν is used, it has values in the interval between -1 and $1/2$, and describes the ratio of lateral contraction to longitudinal strain. For incompressible media the *Poisson* ratio is exactly $1/2$. From equation (3.6) with the shear modulus $G = \frac{Y}{1+\nu}$ in static equilibrium one gets the following set of equations:

$$\frac{\partial \sigma_{ij}}{\partial x_j} = \mathbf{0} \qquad \text{equilibrium of internal forces without external forces,} \tag{3.9}$$

$$\sigma_{ij} = G\left(\frac{\partial u_i}{\partial x_j} + \frac{\partial u_j}{\partial x_i}\right) - p\delta_{ij} = G\varepsilon_{ij} - p\delta_{ij}. \tag{3.10}$$

On top of that, equation (3.7) in the static case for external forces becomes:

$$(1-2\nu) \operatorname{div} \operatorname{grad} \mathbf{u} + \operatorname{grad} \operatorname{div} \mathbf{u} = 0. \tag{3.11}$$

By taking the Laplacian of this equation it gets to the form of a biharmonic equation:

$$\triangle \triangle \mathbf{u} = 0. \tag{3.12}$$

In which $\mathbf{u}$ is a biharmonic (displacement) vector. Finally, a *Greens* function $G(x)$ can be derived from equation (3.12) depending on the boundary conditions of the system considered.

4 Viscoelastic model

In nature, there are nearly no flexible materials that can only be described by viscosity or elasticity. Such materials are therefore called viscoelastic materials. In the following subsections the theoretical foundations for a viscoelastic model, starting with the static case and extending that to dynamics, are presented.

4.1 Static case

In the static case, the set of equations to solve are the momentum balance (3.9) and the stress-strain relation (3.10). The boundary conditions are given by:

$$\sigma_{22}\big|_{x_2=\xi_0} = T(x) + \gamma_s \frac{\partial^2 \xi}{\partial x^2}, \tag{4.1}$$

$$\sigma_{12}\big|_{x_2=\xi_0} = 0, \tag{4.2}$$

$$u_i\big|_{x_2=0} = 0. \tag{4.3}$$

The first equation contains an imposed traction $T(x)$ and the usual curvature pressure term $\gamma_s \frac{\partial^2 \xi}{\partial x^2}$ acting normal to the free top surface and the third equation fixes the bottom surface to a rigid substrate (see figure (8). For this linear system of equations the solution can be obtained by a

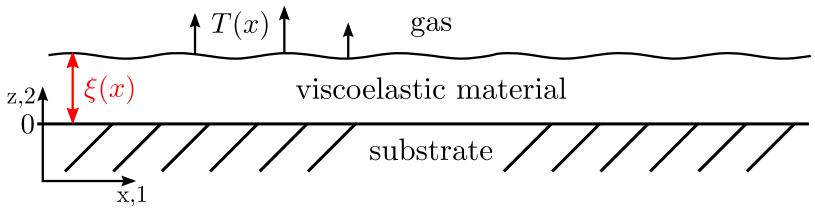

Figure 8: Sketch of the static viscoelastic model showing the imposed traction $T(x)$ on the viscoelastic-gas interface.

convolution of the traction with the *Greens* function $G(x, \Psi_0)$ for the specific elastic medium:

$$\xi(x) = \int_{-\infty}^{\infty} \mathrm{d}x' G(x - x', \Psi_0) \left[T(x') + \gamma_s \frac{\partial^2 \xi}{\partial x'^2} \right]. \tag{4.4}$$

Note that ξ appears on both sides of the equation, so it has to be solved implicitly. The *Green*s function for this system can be obtained by solving the elastostatic equation of the layer with the given boundary conditions. This is a lengthy cumbersome process which does not give any interesting insights, therefore it is not part of this work, but can be found in the literature. [50, 39] It is now convenient to apply a *Fourier* transform in space that is defined by:

$$f(q) = \int_{-\infty}^{\infty} f(x) \exp\left(\mathrm{i}qx\right) \mathrm{d}x, \tag{4.5}$$

$$f(x) = \frac{1}{2\pi} \int_{-\infty}^{\infty} f(q) \exp\left(-\mathrm{i}qx\right) \mathrm{d}q. \tag{4.6}$$

In the next subsections there are more transforms of the same kind, we denote the transformations by the arguments of the functions, here $x \to q$. In detail, the transformation of equation (4.4) is then given by:

$$\int_{-\infty}^{\infty} \xi(x) \mathrm{e}^{\mathrm{i}qx} \, \mathrm{d}x = \int_{-\infty}^{\infty} \int_{-\infty}^{\infty} \mathrm{e}^{\mathrm{i}qx} G(x - x', \Psi_0) \left(T(x') + \gamma_s \frac{\partial^2 \xi(x')}{\partial x'^2} \right) \mathrm{d}x \mathrm{d}x' \tag{4.7}$$

$$= \left(\int_{-\infty}^{\infty} G(\tilde{x}, \Psi_0) \mathrm{e}^{\mathrm{i}q\tilde{x}} \, \mathrm{d}\tilde{x} \right) \int_{-\infty}^{\infty} \left(T(x') + \gamma_s \frac{\partial^2 \xi(x')}{\partial x'^2} \right) \mathrm{e}^{\mathrm{i}qx'} \, \mathrm{d}x' \tag{4.8}$$

where $\tilde{x} = x - x'$. This gives:

$$\begin{aligned} & \xi(q) = G(q, \Psi_0) \left\{ T(q) - \gamma_s \, q^2 \, \xi(q) \right\} \\ \Rightarrow \quad & \xi(q) = \frac{G(q, \Psi_0) \, T(q)}{1 + \gamma_s \, q^2 \, G(q, \Psi_0)}. \end{aligned} \tag{4.9}$$

So, in *Fourier* space and thus in terms of wave vectors, the solution can be written explicitly.

4.2 Dynamic case

In the dynamic case the strain tensor and the stress tensor are time-dependent quantities. We neglect onset effects of the applied force, therefore we are in the overdamped, quasi-static limit $\ddot{u} \to 0$. Then, the tensors still meet the balance of power from the static case (3.9). In order to proceed, the *Boltzmann* superposition principle is used. This is applicable for sufficiently weak forces in which a linear response of the material is expected [14].

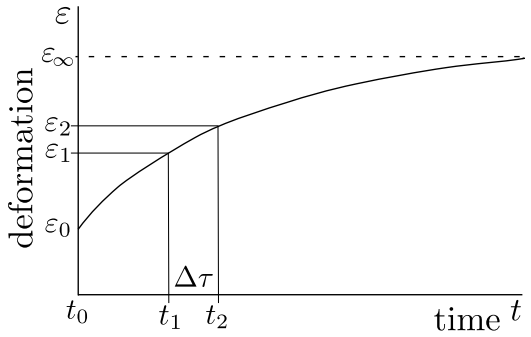

Figure 9: Representation of the time behavior of the deformation of a viscoelastic material when applying a force (creep test). (Adapted from [6])

According to the superposition principle the effects of sequentially executed deformations are additive [6]:

$$\sigma_{ij}(t) = \varepsilon_{ij,0} E(t)\theta(t) + \sum_{n=0}^{N} \frac{(\varepsilon_{ij,n} - \varepsilon_{ij,n-1})}{\Delta\tau} E(t-t_n)\theta(t-t_n), \tag{4.10}$$

where $\theta(t)$ is the *Heaviside* step function and $E(t)$ is the relaxation modulus that contains the temporal part of the deformation tensor ε_{ij}. As the number of subdivisions N goes to infinity, the time difference $\Delta\tau$ goes to zero. The result of this process is a *Duhamel* integral:

$$\sigma_{ij}(t) = \varepsilon_{ij,0} E(t)\theta(t) + \int_{0^+}^{t} \Psi(t-\tau)\partial_\tau \varepsilon_{ij}(\tau)\mathrm{d}\tau. \tag{4.11}$$

The first term on the right hand side can be hidden in the integral by setting the lower limit of the integral to zero. The minus infinity of the lower limit results from the fact that all adaptations of viscoelastic materials to external forces have to be taken into account. Therefore, for the time dependent stress tensor $\sigma_{ij}(t)$ it follows:

$$\sigma_{ij}(x,t) = \int_{-\infty}^{t} \mathrm{d}t' \Psi(t-t') \left[\frac{\partial}{\partial t'} \epsilon_{ij}(x,t')\right] - p(x,t)\delta_{ij}, \tag{4.12}$$

where $\Psi(t)$ is the shear relaxation modulus. This equation is the *Doi-Edwards* constitutive equation for the deformation rate $\partial_t \underline{\underline{\varepsilon}}$. [26] The dynamic response of the subsurface is thus described by a memory core (relaxation modulus), which contains the entire history of the elasto-capillary deformations. The model assumes small curvatures ($(\partial_x h)^2 \ll 1$) [22]. Moreover, in equation (4.12) it is assumed implicitly that $\epsilon_{ij}(t \to -\infty) = 0$. To avoid the convolution in the time dependent equation above, a *Fourier* transform in time is applied:

$$f(\omega) = \int_{-\infty}^{\infty} \mathrm{d}t f(t) \exp(i\omega t), \tag{4.13}$$

$$f(t) = \frac{1}{2\pi} \int_{-\infty}^{\infty} \mathrm{d}\omega f(\omega) \exp(-i\omega t). \tag{4.14}$$

This is possible, if the relaxation modulus $\Psi(t)$ is multiplied by a *Heaviside* step function to cut it off at the upper time integration limit. Performing the transform, the frequency dependent problem is:

$$\frac{\partial \sigma_{ij}(x,\omega)}{\partial x_j} = 0, \tag{4.15}$$
$$\sigma_{ij}(x,\omega) = \mu(\omega)\,\epsilon_{ij}(x,\omega) - p(x,\omega)\,\delta_{ij}.$$

It must comply with the following, also transformed, boundary conditions:

$$\sigma_{2,2}\big|_{x_2=h_0} = T(x,\omega) + \gamma_s \frac{\partial^2}{\partial x^2}\xi(x,\omega), \tag{4.16}$$
$$\sigma_{1,2}\big|_{x_2=h_0} = 0, \tag{4.17}$$
$$u_i\big|_{x_2=0} = 0. \tag{4.18}$$

The main achievement of the temporal *Fourier* transform to derive equation (4.16) is, that the structure of the equations is identical to that of the general static elastic equations (3.10). Thus the solutions of the first system of equations (3.10) also solves this system, if it is transformed accordingly:

$$\xi(q,\omega) = \frac{\frac{G(q)}{\mu(\omega)}\,T(q,\omega)}{1+\gamma_s\,q^2\,\frac{G(q)}{\mu(\omega)}}. \tag{4.19}$$

This equation can be solved individually for each ω and because of its linearity the final solution is a superposition of all ω.

$$\xi(q,\omega) = \frac{G(q)}{\mu(\omega)}\,\sigma_z(q,\omega). \tag{4.20}$$

The transformed relaxation modulus $\mu(\omega)$ is given by:

$$\mu(\omega) = G' + iG'' = -i\omega \int_0^\infty \mathrm{d}t\,\Psi(t)\exp(i\omega t), \tag{4.21}$$

this follows directly from the before mentioned *Fourier* transform of equation (4.12), due to which the time derivative becomes $-i\omega$. It also corresponds to a *Laplace* transform evaluated with $s = -i\omega$. Here, G' is the shear storage modulus which represents the elastic component. The storage modulus is proportional to the deformation energy that is released after the discharge of the material. Furthermore, G'' is the shear loss modulus which represents the viscous component. This corresponds to the converted heat energy by internal friction in the viscoelastic material. Comparing this to models in the literature, the same form also follows from a temporal *Fourier* transform of a model by Matar et al. [28] In their model the *Navier-Stokes* equation (2.20) without the non-linear term (*Stokes* equation) is added to the first elasticity term of the elastic wave equation (3.7) for a

homogenous medium.

$$\rho_s \frac{\partial^2 u_i(t)}{\partial t^2} = -\left(\nabla p_s(t)\right)_i + G \triangle u_i(t) + \mu_s \triangle \left(\frac{\partial u_i(t)}{\partial t}\right), \tag{4.22}$$

$$i\omega^2 \rho_s u_i(\omega) = -\left(\nabla p_s(\omega)\right)_i + \underbrace{(G + i\omega\mu_s)}_{=G'+iG''} \triangle u_i(\omega). \tag{4.23}$$

4.3 Free energy formulation of an elastic model

The free energy of a liquid film with surface profile $h(x,t)$ on top of an elastic substrate of thickness $\xi(x,t)$ is given by:

$$\mathcal{F} = \int_\Omega \left[\frac{\gamma_l}{2} (\nabla h)^2 + \frac{\tilde{\gamma}_s}{2} (\nabla \xi)^2 + f(h-\xi) - h p_h + \frac{\tilde{\kappa}_v}{2} \xi(x) \int_\Omega Q(x-x')\xi(x')\,\mathrm{d}x' \right] \mathrm{d}x, \tag{4.24}$$

where $Q(x) = G^{-1}(x)$ is the inverse *Greens* function. The contributions are, respectively: energy of the liquid-gas interface, energy of the solid-liquid interface, wetting energy, Lagrange multiplier to ensure mass conservation of liquid layer for static films and elastic energy. Since $Q(x)$ diverges for incompressible media we need to go to a compressible medium with *Poisson* ratio $\nu < 1/2$. The elastic energy involves a convolution with a symmetric kernel $Q(x)$, which is simplified in the following. For $Q(x=0) = 0$ the *Taylor* series of $\xi(x')$ around x of the inner integral (local approximation) is given by:

$$\begin{aligned} \int Q(x-x')\xi(x')\,\mathrm{d}x' \approx \xi(x) \int Q(\tilde{x})\,\mathrm{d}\tilde{x} + \frac{\mathrm{d}\xi}{\mathrm{d}x} \int Q(\tilde{x})\tilde{x}\,\mathrm{d}\tilde{x} + \frac{1}{2}\frac{\mathrm{d}^2\xi}{\mathrm{d}x^2} \int Q(\tilde{x})\tilde{x}^2\,\mathrm{d}\tilde{x} \\ + \frac{1}{6}\frac{\mathrm{d}^3\xi}{\mathrm{d}x^3} \int Q(\tilde{x})\tilde{x}^3\,\mathrm{d}\tilde{x} + \frac{1}{24}\frac{\mathrm{d}^4\xi}{\mathrm{d}x^4} \int Q(\tilde{x})\tilde{x}^4\,\mathrm{d}\tilde{x} + \mathcal{O}(\tilde{x}^5) \end{aligned} \tag{4.25}$$

If $Q(\tilde{x})$ is an even function ($Q(\tilde{x}) = Q(-\tilde{x})$) the terms of odd order in derivatives of ξ vanish. The second order term renormalizes the surface energy

$$\gamma_s = \tilde{\gamma}_s - \frac{\tilde{\kappa}_v}{2} \int Q(\tilde{x})\tilde{x}^2\,\mathrm{d}\tilde{x} \tag{4.26}$$

and the fourth order term gives a further stabilizing contribution to the energy that corresponds to a bending energy $(\triangle\xi)^2$.

Variations for a 1D system, where $\Pi_I(h-\xi) = -\partial_I f(h-\xi)$ and $I = \{h, \xi\}$, give:

$$\frac{\delta \mathcal{F}}{\delta h} = -\gamma_l \frac{\mathrm{d}^2}{\mathrm{d}x^2} h + \Pi_h(h-\xi) = p_h, \tag{4.27}$$

$$\frac{\delta \mathcal{F}}{\delta \xi} = -\tilde{\gamma}_s \frac{\mathrm{d}^2}{\mathrm{d}x^2} \xi - \Pi_\xi(h-\xi) + \tilde{\kappa}_v \int Q(x-x')\xi(x')\,\mathrm{d}x' = 0. \tag{4.28}$$

The second equation is in local approximation (even Q)

$$-\gamma_s \frac{\mathrm{d}^2}{\mathrm{d}x^2} \xi - \Pi_\xi(h-\xi) + \kappa_{v0}\,\xi + \kappa_{v4} \frac{\mathrm{d}^4}{\mathrm{d}x^4} \xi = \kappa_{v0}\,\xi_0 \tag{4.29}$$

with

$$\kappa_{v0} = \frac{\tilde{\kappa}_v}{2} \int Q(\tilde{x})\,\mathrm{d}\tilde{x} \quad \text{and} \quad \kappa_{v4} = \frac{\tilde{\kappa}_v}{24} \int Q(\tilde{x})\tilde{x}^4\,\mathrm{d}\tilde{x}. \tag{4.30}$$

The *van der Waals* interaction together with *Born* repulsion [34] give a disjoining pressure of

$$\Pi_I(h-\xi) = \frac{1}{(h-\xi)^3}\left(1 - \left(\frac{h_{pc}}{h-\xi}\right)^3\right). \tag{4.31}$$

It should be noted that we only consider interactions between the two layers h and ξ and there are no interactions with the rigid substrate, this is a thick film limit for ξ. It means that the viscoelastic layer ξ is thick enough that the interactions with the rigid substrate do not contribute to the form of its interface with the liquid layer h. For the numerical calculation the simple form $Q(x) = \delta(x)$ and $h_{pc} = 1$ are used, therefore the parameters in equation (4.30) are given by $\kappa_{v0} = \frac{\tilde{\kappa}_v}{2}$ and $\kappa_{v4} = 0$, so that

$$\kappa_v \int Q(x-x')\xi(x')\mathrm{d}x' = \kappa_v(\xi(x) - \xi_0). \tag{4.32}$$

This can be interpreted as one big spring in the elastic lower layer.

5 Basics of polymer models

For the characterization of polymers there are two different experimental tests: The relaxation test, and the creep test. The relaxation test is carried out by a constant deformation to the material in which then a tension builds. This tension decreases in viscoelastic materials, such as polymers, over time and either goes to zero or to a constant. For the creep test often a heavy block is applied to the viscoelastic material, then the deformation of the material at the constant load is measured. The deformation then increases to a constant for long measurement times. Theoretically, one determines (analogous to *Hooke*'s law) the relaxation modulus $E(t)$ like this:

$$\sigma_{ij}(t) = E(t)\varepsilon_{ij,0}, \tag{5.1}$$

and the creep compliance $D(t)$ as:

$$\varepsilon_{ij} = D(t)\sigma_{ij,0}. \tag{5.2}$$

With these tests, you can check the linearity of the material by changing $\varepsilon_{ij,0}$ and respectively $\sigma_{ij,0}$. For comparison to classical mechanics viscoelastic materials such as polymers are often described by spring and damper models. Using the standard relations for linear materials and the stress tensors for springs σ_S and dampers σ_D, one gets:

$$\sigma_S = E\varepsilon_S, \qquad \sigma_D = \eta\dot{\varepsilon}_D. \tag{5.3}$$

The spring represents the elastic component and the damper the viscous component of the material. For parallel "circuits" one has in general:

$$\sigma = \sigma_1 + \sigma_2, \qquad \varepsilon = \varepsilon_1 = \varepsilon_2, \tag{5.4}$$

while for series "circuits" it is [6]:

$$\sigma = \sigma_1 = \sigma_2, \qquad \varepsilon = \varepsilon_1 + \varepsilon_2. \tag{5.5}$$

One can obtain differential equations for the time evolution of the tensors from material models build from combinations of the before mentioned "circuits".

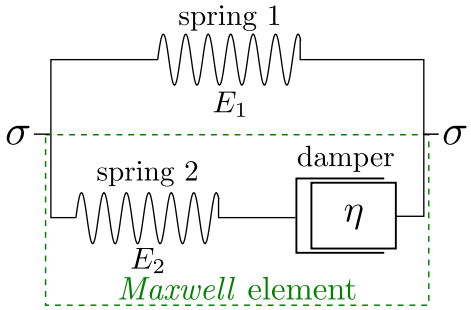

Figure 10: Sketch of the mechanical diagram for the *Standard Linear Solid* model.

In case of the *Standard Linear Solid* model defined for example in [22] and shown in figure (10) one has:

$$\sigma_M = \sigma_{S2} = \sigma_D, \qquad \varepsilon_M = \varepsilon_{S2} + \varepsilon_D, \quad \textit{Maxwell} \tag{5.6}$$

$$\sigma = \sigma_M + \sigma_{S1}, \qquad \varepsilon = \varepsilon_M = \varepsilon_{F1}. \tag{5.7}$$

By deriving with respect to time and substituting the following result is produced:

$$\begin{aligned}
\dot{\varepsilon} =& \dot{\varepsilon}_{S2} + \dot{\varepsilon}_D, \\
=& \frac{\dot{\sigma}_M}{E_2} + \frac{\sigma_D}{\eta}, \\
=& \frac{\dot{\sigma}_M}{E_2} + \frac{\sigma_M}{\eta}, \\
=& \frac{\dot{\sigma} - \dot{\sigma}_{S1}}{E_2} + \frac{\sigma - \sigma_{S1}}{\eta}, \\
=& \frac{1}{E_2}\dot{\sigma} - \frac{E_1}{E_2}\dot{\varepsilon} + \frac{1}{\eta}\sigma - \frac{E_1}{\eta}\varepsilon, \\
=& \frac{1}{E_1 + E_2}\left(\dot{\sigma} + \frac{E_2}{\eta}\sigma - \frac{E_1 E_2}{\eta}\varepsilon\right).
\end{aligned} \tag{5.8}$$

In this model the relaxation time is given by $\tau = \frac{\eta}{E_2}$. The solution of the differential equation is obtained by using a *Laplace* transform. In the end, one gets the relaxation function $\Psi(t)$ that describes the time evolution of the tensor:

$$\Psi(t) = \frac{\sigma(t)}{\varepsilon_0} = \left(E_1 + E_2 \mathrm{e}^{-\frac{t}{\tau}}\right). \tag{5.9}$$

6 Results produced with auto07p

In this work the numerical tool *auto07p* is used for the continuation of the different models [10]. Continuation of a nonlinear system of n equations $F(\mathbf{y}, \lambda) : \mathbb{R}^n \times \mathbb{R} \mapsto \mathbb{R}^n$ is used to determine the dependence of a stationary state of the model $F(\mathbf{y}, \lambda) = 0$ on a parameter λ. Therefore, it can be used to construct the bifurcation diagram of the model depending on the chosen parameter. A sufficiently differentiable system of equations defines a smooth one-dimensional manifold (curve) $\mathcal{M} \in \mathbb{R}^n \times \mathbb{R}$ [23] (see figure (11)). In general, continuation starts from an initial state $F(\mathbf{y}_0 = \mathbf{y}(\lambda_0), \lambda_0)$ that is

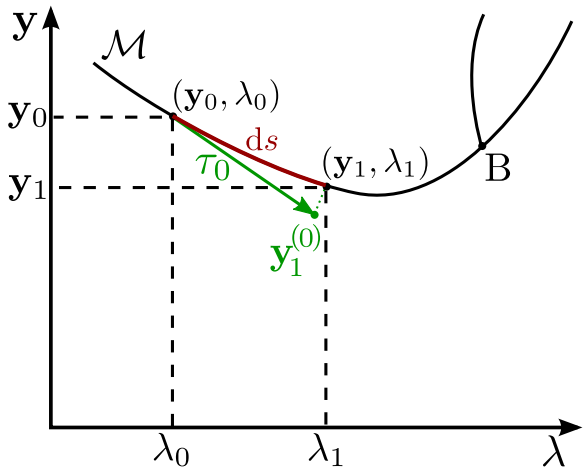

Figure 11: Sketch of the pseudoarclength continuation. The point B denotes a branching point in which there are two possible ways to continue the path. (Resketched and adapted from [23])

sufficiently close to or on this curve and then tries to predict the next direction in that the curve extends and a step of size ds is made in this direction. Following this, an iterative solver is used to get the first approximation of a solution by the predictor back on the curve. This is why such numerical methods are called predictor-corrector methods. One example is the natural continuation, but its predictor is given by a step in the continuation parameter $\Delta\lambda$ so the solution given by the corrector at constant λ cannot converge, if the curve has a fold.

In contrast, the continuation technique used here depends on a pseudoarclength defined as an approximation of the curve $\mathcal{M}$ in its tangent space. This ensures that the solution produced by the predictor for small enough steps ds is always close enough to the curve to let a *Newton* method converge. Because of this tangent approach it also works for curves with folds as the predicted solutions are always nestled close to the solution curve. Hence, it is more stable which can be used in a larger step size ds than in the natural continuation method. The pseudoarclength approach

uses the following algorithm [9]:

1. Predictor: Use the normalized tangent τ scaled with the step size $\mathrm{d}s$ to get new solution:

$$(\mathbf{y}_{i+1}^{(*)}, \lambda_{i+1}^{(*)}) = (\mathbf{y}_i, \lambda_i) + \tau_i \, \mathrm{d}s. \tag{6.1}$$

2. Corrector: Use an iterative solver, in this case *Newton* method, to get back to the curve:

$$\frac{\partial F}{\partial \mathbf{y}}(\mathbf{y}_{i+1}^{(\nu)}, \lambda_{i+1}^{(\nu)}) \, \Delta\mathbf{y}_{i+1}^{(\nu)} = -F(\mathbf{y}_{i+1}^{(\nu)}, \lambda_{i+1}), \quad \text{with } \Delta\mathbf{y}_{i+1}^{(\nu)} = \mathbf{y}_{i+1}^{(\nu+1)} - \mathbf{y}_{i+1}^{(\nu)}, \tag{6.2}$$

   where $\nu \in \mathbb{N}_0$ is the number of iterations.

3. Construct the new tangent τ_{i+1}:

$$\tau_{i+1} = \frac{\mathrm{d}}{\mathrm{d}s}(\mathbf{y}(s), \lambda(s))\Big|_{s=s_{i+1}}. \tag{6.3}$$

Then repeat the processes 1-3 to walk in steps of Δs along the path defined by the curve. Then, the underlying curve can be reproduced by joining the computed solution points. Such a curve can contain branching points, so in general more elaborate algorithms to be able to switch at such points are used (see point B in figure (11)). Given the complexity of the advanced algorithms the presented explanation should suffice in the scope of this work.

In the following paragraph some basic information for the understanding of the following subsections is given. In default settings, *auto07p* uses the L^2-norm $\|h\|_{L^2}$, it reads:

$$\|h\|_{L^2} = \left(\int_\Omega (h(x) - h_0)^2 \, \mathrm{d}x \right)^{\frac{1}{2}}. \tag{6.4}$$

Moreover, to show the dependence on the number of drops in the volume a drop period d_p is defined.

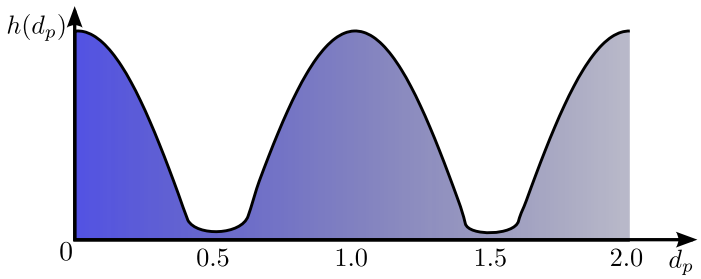

Figure 12: Sketch showing the definition of the drop period d_p used in the auto subsection.

It should be clear from figure (12) that the drop period d_p is always a positive multiple of 0.5 and represents the number of drops in the system domain Ω. Since *auto07p* can only work with ordinary

differential equations the thin film equation has to be set to the static case $\partial_t h = 0$:

$$\frac{\partial}{\partial t} h = \nabla \cdot [Q(h) \nabla p(h)] \stackrel{!}{=} 0, \quad \left| \int_\Omega (\cdot)\, \mathrm{d}x \right. \tag{6.5}$$

$$Q(h) \nabla p(h) = \mathbf{J}_0 = 0, \quad \left| : Q(h),\ \int_\Omega (\cdot)\, \mathrm{d}x \right. \tag{6.6}$$

$$p(h) = p_h. \tag{6.7}$$

Since the terms in the brackets are a convective flow, the first integration constant is a flow $\mathbf{J}_0$ that can be set to zero because it represents an outgoing flow that has to be dropped for the system to be closed. The mobility $Q(h)$ expresses a property of moving fluids, so it should be no surprise that it is dropped in the static case. This is done by a division after the first integration (6.6) which is also always defined because the mobility $Q(h)$ is always nonzero and for thin films with multiple layers a positive semi-definite matrix (see subsection (2.5)). The second integration constant is given by the external pressure p_h that balances the internal pressure and can be used by *auto07p* as a free parameter for continuation. This transformation to the static equation drops the continuity structure of the time dependent thin film equation and thus a integral condition to account for mass conservation for each layer is needed, it reads:

$$\Psi_{i,0} = \frac{1}{\Omega} \int_\Omega \Psi_i(x)\, \mathrm{d}x, \tag{6.8}$$

wherein $\Psi(x)$ represents a vector of the layers and Ψ_0 is a vector of the mean heights of the layers that can be used as continuation parameters.

As should be clear from the theoretical background to continuation methods, an initial solution $F(y_0, \lambda_0)$ close to or exactly representing a real solution of the differential equation is needed to start a continuation. This is the main concern in working with *auto07p* on more elaborate models. Because as the model increases in complexity to account for all physical conditions, the equations are usually only approximately analytically solvable. Since the main structure of solution relevant for this topic is a drop shape, the initial solution is approximated by a sinusoidal function with a small amplitude $A \ll 1$:

$$h = -A \cos(2\pi d_p x), \tag{6.9}$$

$$h' = 2\pi A d_p \sin(2\pi d_p x). \tag{6.10}$$

If the model is described by two fields the signs can be switched for the lower layer to describe the counter-structure to the top layer structure. This simplification works sufficiently in view of the models in this thesis, although the solution did not converge for higher drop numbers $d_p > 0.5$

for the radial elastic model. Due to the equations in this model that have a *Bessel* differential equation structure a solution with *Bessel* functions should converge. Following this inspiration, a few tests have been performed that concluded without any success in convergence. Therefore a more sophisticated method has been developed to switch to the solution branches with higher drop numbers as can be read in the subsection (6.2).

6.1 Simple elastic model

The simple elastic model is given by the free energy (4.24). Following the arguments of subsection (4.3) the static coupled equations to use for continuation read:

$$-\gamma_l \frac{\mathrm{d}^2}{\mathrm{d}x^2} h(x) + \Pi_h(h(x) - \xi(x)) = p_h, \tag{6.11}$$

$$-\gamma_s \frac{\mathrm{d}^2}{\mathrm{d}x^2} \xi(x) - \Pi_\xi(h(x) - \xi(x)) + \kappa_v(\xi(x) - \xi_0) = p_\xi. \tag{6.12}$$

The program can only work with first order differential equations, so a transformation is needed that is shown here only for equation (6.11):

$$\zeta = \frac{x}{L}, \quad u_1 = h - h_0 \quad u_2 = \frac{\mathrm{d}h}{\mathrm{d}x}. \tag{6.13}$$

This gives us the following equations (NDIM=4):

$$\frac{\mathrm{d}u_1}{\mathrm{d}\zeta}(x) = L\left(\frac{\mathrm{d}h}{\mathrm{d}x}\right), \tag{6.14}$$

$$\frac{\mathrm{d}u_2}{\mathrm{d}\zeta}(x) = L\left(\Pi_h - p_h\right), \tag{6.15}$$

$$\frac{\mathrm{d}u_3}{\mathrm{d}\zeta}(x) = L\left(\frac{\mathrm{d}\xi}{\mathrm{d}x}\right), \tag{6.16}$$

$$\frac{\mathrm{d}u_4}{\mathrm{d}\zeta}(x) = L\left(\Pi_\xi + \kappa_v(\xi - \xi_0) - p_\xi\right)/\sigma. \tag{6.17}$$

In which the ratio of interface tensions is given by $\sigma = \frac{\gamma_l}{\gamma_s}$. The equations also have four boundary conditions (for h, h', ξ, ξ') that are all chosen to be periodic (NRB = 4). Since the integration drops the continuity character of the equation two integral conditions for mass conservation of both layers are needed (NINT = 2), see equation (6.8). Following this, the program needs three continuation parameters: NCONT = (NRB=4) + (NINT=2) - (NDIM=4) + 1 = 3. These are both pressures p_h and p_ξ as well as one parameter in which the continuation is done. In figure (13) the continuation parameter is κ_v and shown are solutions of the equations for four different values of κ_v. For an decreasing vertical compression elasticity κ_v the elastic medium gets more fluid and in the limit of

$\kappa_v \to 0$ the equations become the standard equations for two fluid films given by:

$$-\gamma_{l_1} \frac{\mathrm{d}^2}{\mathrm{d}x^2} h(x) + \Pi_h(h(x) - \xi(x)) = p_h, \tag{6.18}$$

$$-\gamma_{l_2} \frac{\mathrm{d}^2}{\mathrm{d}x^2} \xi(x) - \Pi_\xi(h(x) - \xi(x)) = p_\xi. \tag{6.19}$$

The solutions of this system are well known and look like a lense shape in which the upper film is vertically mirrored in the lower film. This sort of behavior can also be reproduced by the model. It is important to note, that the model also shows the bulges at the contact point of the drop with

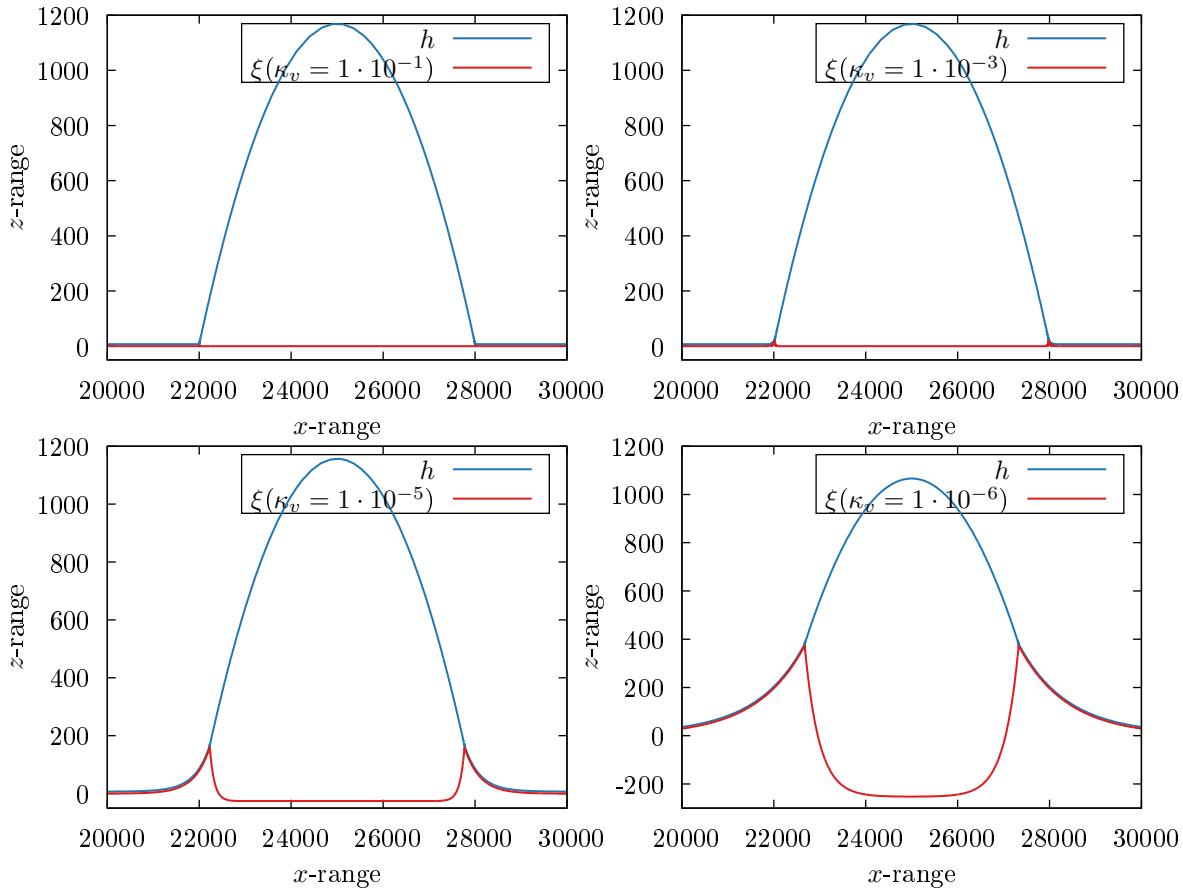

Figure 13: Solutions of the static model for four different values of vertical compression elasticity κ_v at domain size of L=$5{\cdot}10^4$, $h_0 = 100$ and $\sigma = \frac{\gamma_l}{\gamma_s} = 0.1$. The plot shows only part of the domain size.

the substrate and one can also see the effect of the *Laplace* pressure pushing the substrate down under the layer. For the other limit $\kappa_v \to \infty$ the substrate becomes rigid as one can see in the in

the figure corresponding to $\kappa_v = 1 \cdot 10^{-1}$, in which the bulges produced by the capillary force at the contact region are suppressed. This can also be seen in the form of the bifurcation diagram (14) as it is identical to that of a drop on a solid surface. To compare both diagrams and the solutions the mean thickness ξ_0 of the (in)elastic substrate has to be subtracted from the height of the liquid film h. The continuation starts at a value near zero of the mean height h_0 of the liquid film and then a

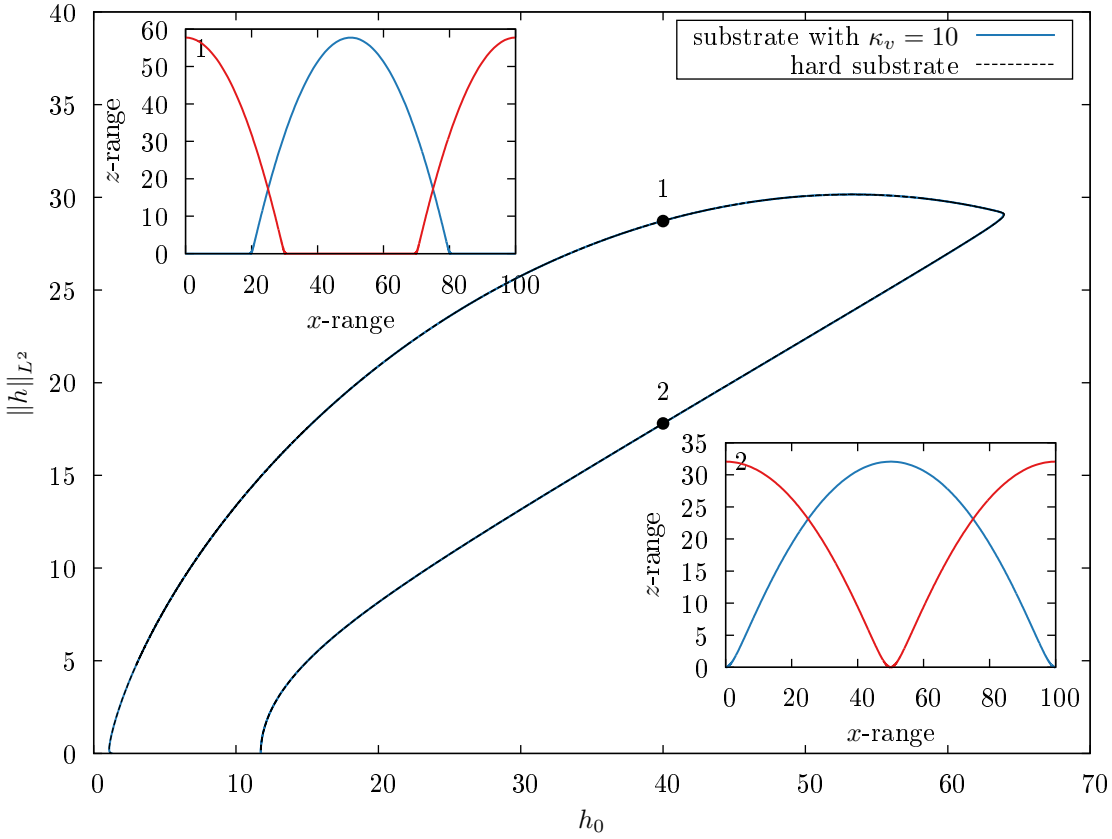

Figure 14: Bifurcation diagram for a high vertical compression elasticity $\kappa_v = 10$ compared to that of a drop on a hard surface. The system is contained in a domain of size $L = 100$. Comparing both of this curves one can see that they are identical and also the solutions at a mean height $h_0 = 40$, which are depicted in the boxes, look exactly the same. The two colors in the solution boxes indicate two different kind of solutions the red solutions have a hole in the center and a drop at the boundaries of the domain. The blue solutions are the same except that the drop is in the center.

supercritical bifurcation occurs and continuation follows the branch upwards around the curve. At the fold of the curve the maximum drop size of the chosen domain size $L = 100$ is reached so the

drop touches the boundary or itself in the center and the norm begins to decrease as it gets flatter. When the curve goes to zero in the L^2-norm it indicates that a flat film is reached and the solution switches between the solutions (red, blue) shown in figure (14).

6.1.1 Contact angle

The solid-liquid angle θ_{sl} of the liquid film $h(x)$ with an elastic substrate $\xi(x)$ has to change with the compression elasticity κ_v. As one would expect this dependence also changes with the ratio of the surface tensions $\sigma = \frac{\gamma_l}{\gamma_s}$ of the involved materials. This dependence is shown in figure (15).

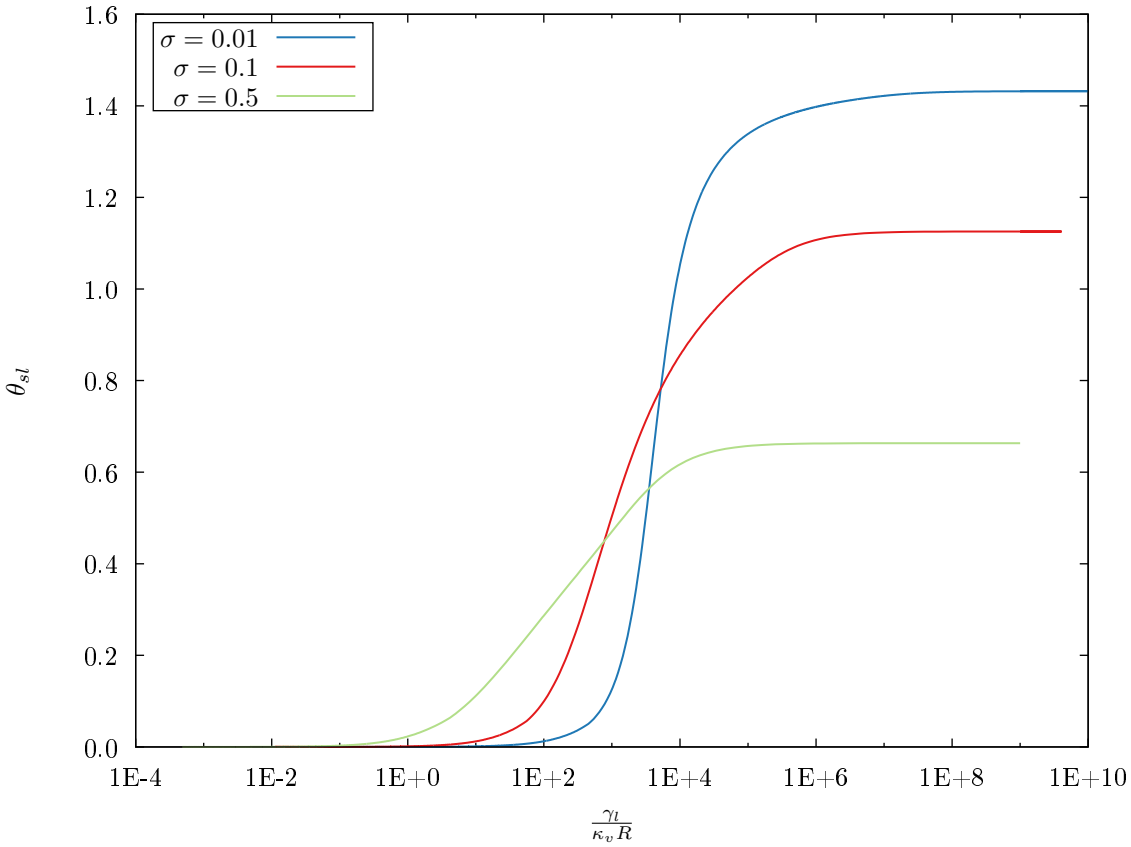

Figure 15: Dependence of the angle θ_{sl} on the dimensionless softness parameter $\frac{\gamma_l}{\kappa_v R}$ for different values of $\sigma = \frac{\gamma_l}{\gamma_s}$ at a domain size of $L = 500$.

At first glance, the graph shows two constant plateaus of the angle θ_{sl} (see figure (16)) that are asymptotically reached for either high or low numbers of the softness parameter $\frac{\gamma_l}{\kappa_v R}$. This quan-

tity is inverse proportional to the vertical compression elasticity κ_v. Throughout this continuation the liquid surface tension is constant $\gamma_l = 1.0$ and the drop radius R changes negligible compared to the constant κ_v, therefore the contact angle θ_{sl} is depending directly on $\frac{1}{\kappa_v}$ in this graph. The plateaus mentioned before are based on the fact that for high vertical compression elasticity κ_v the elastic medium behaves like a solid and thus the angle θ_{sl} goes to zero. For low values of κ_v the elastic medium increases in fluidity and asymptotically the size of the angle θ_{sl} is depending only on the ratio of the surface tensions of the "liquids" σ like in liquid-liquid films. The main result of the figure is that the higher the ratio of surface tensions σ gets, the lower the asymptotic angle for low κ_v gets. Another conclusion from it is given by the fact that the slope of the approximately linear behavior between the constant ends of the curves also decreases if σ increases. In correlation to the decreasing slope of the curves, the width of the transition interval from hard to fluid lower layer increases with σ.

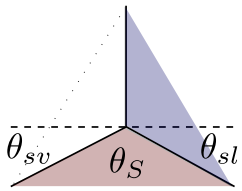

Figure 16: Sketch of the definition of the angle θ_{sl} to be consistent with [27].

6.2 Radial elastic model

Since drops without external forces tend to be axisymmetric (see figure (17)) the equations are transformed into cylindrical symmetry.

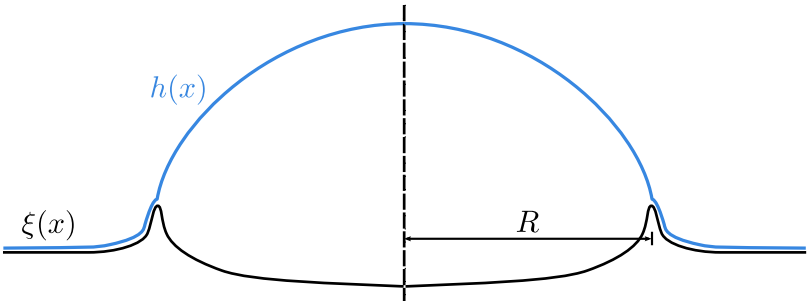

Figure 17: Sketch of an axisymmetric drop on a soft substrate ξ.

Therefore, the free energy functional $\mathcal{F}$ of this model, wherein the functional determinant r is given by the symmetry, is given by:

$$\mathcal{F}[h(r),\xi(r)] = 2\pi \int_\Omega \left[\frac{\gamma_l}{2} \left(\frac{\mathrm{d}h}{\mathrm{d}r} \right)^2 + \frac{\gamma_s}{2} \left(\frac{\mathrm{d}\xi}{\mathrm{d}r} \right)^2 + \frac{\kappa_v}{2} (\xi - \xi_0)^2 + f(h-\xi) + p_h h \right] r \, \mathrm{d}r. \tag{6.20}$$

Minimizing this functional with respect to the layer heights $h(r)$ and $\xi(r)$ gives us the model:

$$-\gamma_l \left(\frac{\mathrm{d}^2}{\mathrm{d}r^2} h(r) + \frac{1}{r} \frac{\mathrm{d}}{\mathrm{d}r} h(r) \right) + \Pi_h(h(r) - \xi(r)) = p_h, \tag{6.21}$$

$$-\gamma_s \left(\frac{\mathrm{d}^2}{\mathrm{d}r^2} \xi(r) + \frac{1}{r} \frac{\mathrm{d}}{\mathrm{d}r} \xi(r) \right) - \Pi_\xi(h(r) - \xi(r)) + \kappa_v(\xi(r) - \xi_0) = p_\xi. \tag{6.22}$$

Here, p_h and p_ξ are the pressures in the upper and lower film which can be used as free continuation parameters. Again, these equations have to be transformed into first order differential equations and one gets:

$$\frac{\mathrm{d}u_1}{\mathrm{d}\zeta}(r) = L \left(\frac{\mathrm{d}h}{\mathrm{d}r} \right), \tag{6.23}$$

$$\frac{\mathrm{d}u_2}{\mathrm{d}\zeta}(r) = L \left(-\frac{\alpha \, \mathrm{d}_r h}{\alpha r + 1.0 - \alpha} - \Pi_h - p_h \right) \tag{6.24}$$

$$\frac{\mathrm{d}u_3}{\mathrm{d}\zeta}(r) = L \left(\frac{\mathrm{d}\xi}{\mathrm{d}r} \right) \tag{6.25}$$

$$\frac{\mathrm{d}u_4}{\mathrm{d}\zeta}(r) = L \left(-\frac{\alpha \, \mathrm{d}_r \xi}{\alpha r + 1.0 - \alpha} - \Pi_\xi - p_\xi \right) / \sigma \tag{6.26}$$

$$\frac{\mathrm{d}u_5}{\mathrm{d}\zeta}(r) = L. \tag{6.27}$$

There is some explanation needed for the use of the rather complex fraction containing the first derivatives d_r and α. The parameter $\alpha \in [0, 1)$ allows for a continuous transition (homotopy) from *Cartesian* coordinates to cylindrical coordinates. This is expressed by the functional form of the fraction $\frac{\alpha f(r)}{(\alpha r + 1.0 - \alpha)}$ and is needed because the domain is normed to the interval $[0, 1]$ in *auto07p* that produces undefined behavior for the division $\frac{1}{r}$ needed at $r = 0$. Hence, in using the continuation for this model one run is needed to switch on the correct symmetry $\alpha : 0 \to 1$ to get the program to perform a 2D-continuation. Moreover, because of the new symmetry the boundary conditions, to solve the system of equations (6.27), change to:

$$h(r)@ \text{ left boundary} = 0, \tag{6.28}$$

$$\frac{\mathrm{d}h(r)}{\mathrm{d}r}@ \text{ right boundary} = 0, \tag{6.29}$$

$$\xi(r)@ \text{ left boundary} = 0, \tag{6.30}$$

$$\frac{\mathrm{d}\xi(r)}{\mathrm{d}r}@ \text{ right boundary} = 0, \tag{6.31}$$

$$r@ \text{ left boundary} = 0. \tag{6.32}$$

The free energy of a flat film $\mathcal{F}_{\mathrm{fl.f}}$ is given by:

$$\mathcal{F}_{\mathrm{fl.f}} = 2\pi \int_\Omega f(h_0 - \xi_0) r \, \mathrm{d}r, \tag{6.33}$$

this can be substracted from equation (6.20) to get the relative free energy $\mathcal{F}_{\text{rel.}}$. For a domain size of $L = 500$, a ratio of surface tensions $\sigma = 0.1$ and a compression elasticity $\kappa_v = 0.001$ the bifurcation and energy diagram is shown in figure (18) for a drop number of $d_p = 0.5$.

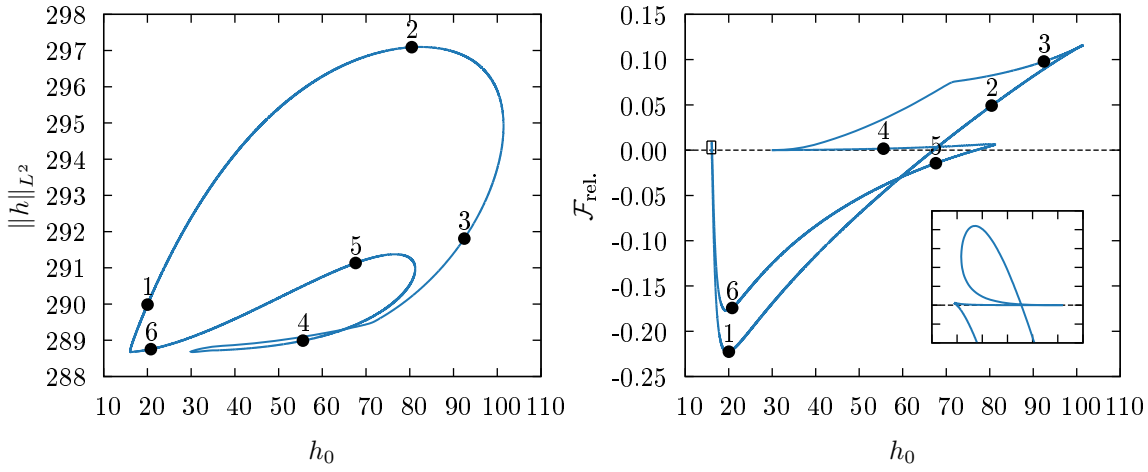

Figure 18: Bifurcation diagram for drop number $d_p = 0.5$ of the elastic model in polar geometry. Left: L^2-norm depending on the mean height of the upper layer h_0. Right: Relativ free energy $\mathcal{F}_{\text{rel.}}$ as a function of the mean height of the upper layer h_0. The points correspond to solutions shown on the next page and the small rectangle in the right graph shows the area that is zoomed in the small graph. For these diagrams, the domain size is $L = 500$, the surface tension ratio $\gamma = 0.1$ and the vertical compression elasticity $\kappa_v = 0.001$.

As one can see, the bifurcation diagram showing the L^2-norm depending on the mean height of the upper layer h_0 starts before label 1 with a supercritical bifurcation and then follows the curve to form a closed loop. There is also one knot visible in which the solutions have the same L^2-norm but a different type of structure, one has a drop and the other has a hole in the center and thus forms a target structure. The corresponding solutions to the diagrams are shown in figure (19). Following the bifurcation curve along the labels with the arclength s and plotting the height of the liquid and the position of the ridge depending on this arclength one gets figure (20). A conclusion from the figure is that the highest drop does not correspond to the widest drop. As the drop increases its mean height at first the drop height increases faster than the radius but at an arclength of $s = 0.372$ the height begins to decrease and the radius continues to increase, but slower than before. In general, it is clear to see from figure (20) that the radius increases linear with the mean height of the upper film till the contact line reaches the boundary. Then the afore mentioned switch of solution occurs

and the radius begins to decrease again but this time the drop sits at the outer boundary as a hole is formed in the center.

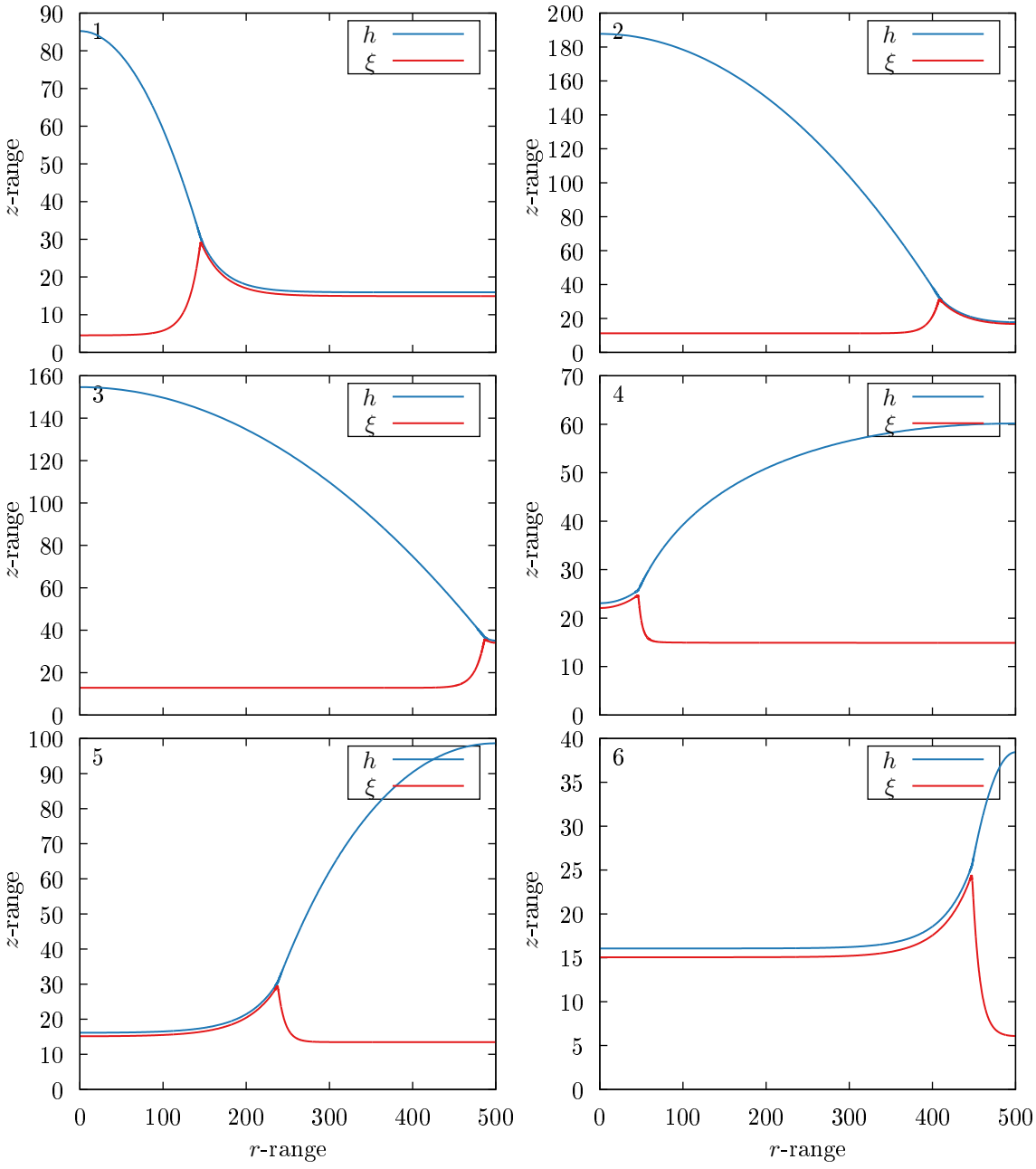

Figure 19: Solutions of the radial elastic model at domain size of L=500, $\sigma = \frac{\gamma_l}{\gamma_s} = 0.1$ and a compression elasticity of $\kappa_v = 0.001$.

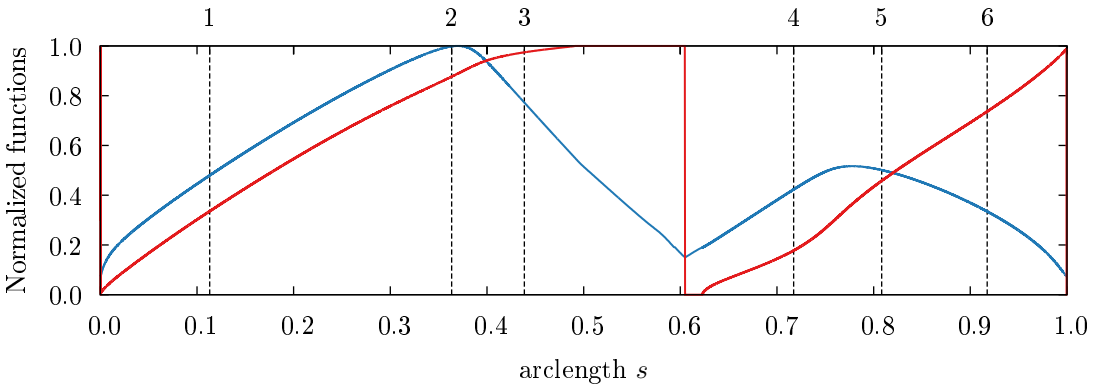

Figure 20: Height of the upper drop $h_{\max}$ (blue) and r at the ridge $r@\xi_{\max}$ (red) in dependence of the arclength s. The vertical dashed lines show where the solutions are found in this plot and their labels are at the top x-axis.

Since the solutions are radial symmetric they can also be plotted in 3D space like in the following figure (21) produced with *Mathematica*.

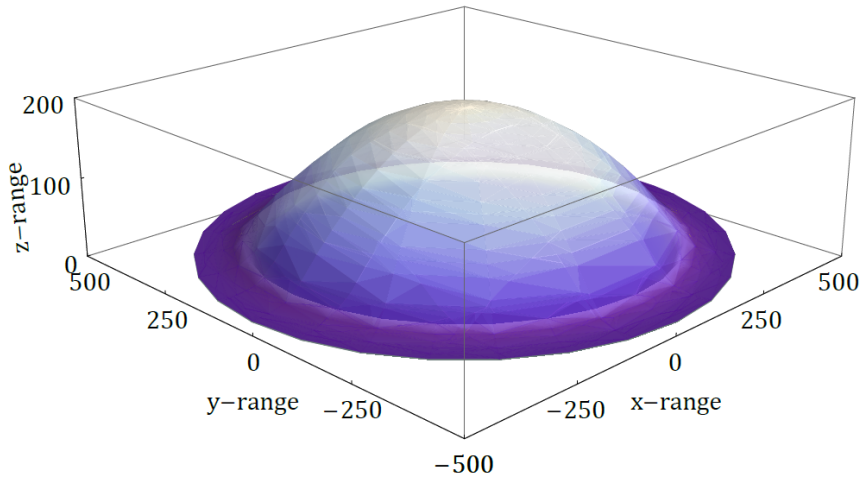

Figure 21: 3D plot of the radial symmetric solution 2. The domain size is $L = 500$, the ratio of interface tensions is $\sigma = 0.1$ and the vertical compression elasticity is $\kappa_v = 0.001$. In the surface plot one can clearly see the ridge that has formed at the contact line of the drop with the substrate. This figure is produced with *Mathematica* using the function RevolutionPlot3D.

Furthermore, it is also possible to produce the bifurcation diagrams for solutions with higher drop numbers. This can be achieved by starting with the solution produced in the first run with drop number $d_p = 0.5$ and then continuing in the derivative at the right boundary C_D. To incorporate

this into the code, the following change has to be made to the boundary conditions:

$$\frac{\mathrm{d}h(r)}{\mathrm{d}r}@ \text{ right boundary} = C_D, \tag{6.34}$$

$$\frac{\mathrm{d}\xi(r)}{\mathrm{d}r}@ \text{ right boundary} = C_D. \tag{6.35}$$

Continuing in the parameter C_D increases the derivative to a number until a sign change occurs in C_D and the derivative decreases. This process happens periodically and while this happens the solutions for the fields h and ξ are forced to adapt to the changes. Hence it is possible for the solutions to switch branch to higher drop numbers $d_p > 0.5$ as is shown in figure (22).

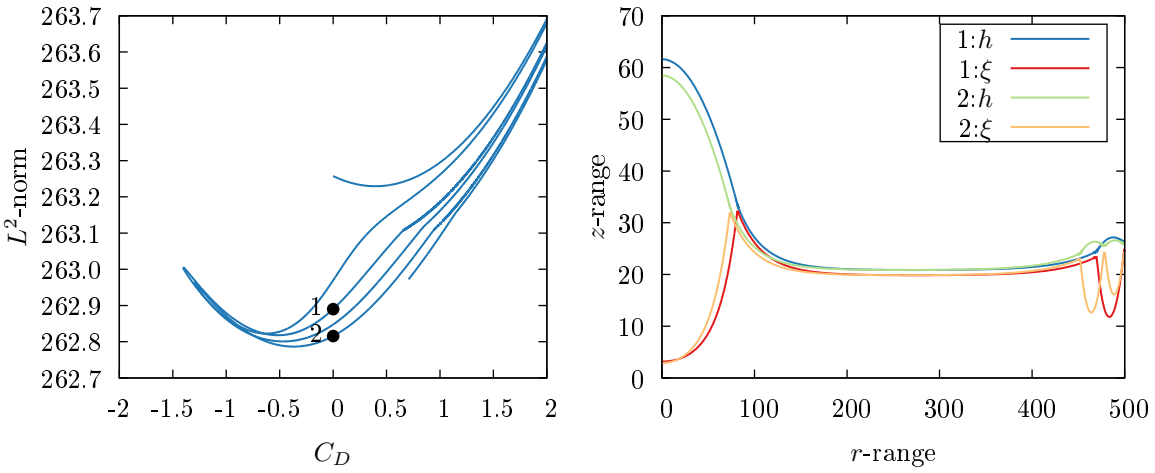

Figure 22: Left: L^2-norm in dependence of continuation parameter of derivative at right boundary C_D. The curve extends till $C_D = 8.0$, but nothing interesting happens so it is cropped to the shown region. Right: Solutions at the labels 1 and 2 to show the added drops at the boundary. Representation of the technique to switch branches to higher drop numbers $d_p > 0.5$ for the radial elastic model. Each swing through the zero value of C_D adds 0.5 to the drop number d_p.

Similar to this, the technique is also used and has been developed in the much simpler model for just an axisymmetric drop on a rigid substrate (see appendix B). Each swing through the zero value of the continuation parameter of the derivative at the right boundary C_D adds a drop number of $d_p+ = 0.5$ to the existing drop number. The solutions in the plot show the two solutions which are further used in continuation by increasing the top layer thickness h_0. The form of the relative free energy $\mathcal{F}_{\text{rel.}}$ plot in the upper right quadrant is produced by the fact that the domain size of $L = 500$ is too small for this drop number $d_p = 1.5$. Since the drops touch the boundary shortly after the start of the continuation they tend to increase only in h_0 and therefore it has a stretching

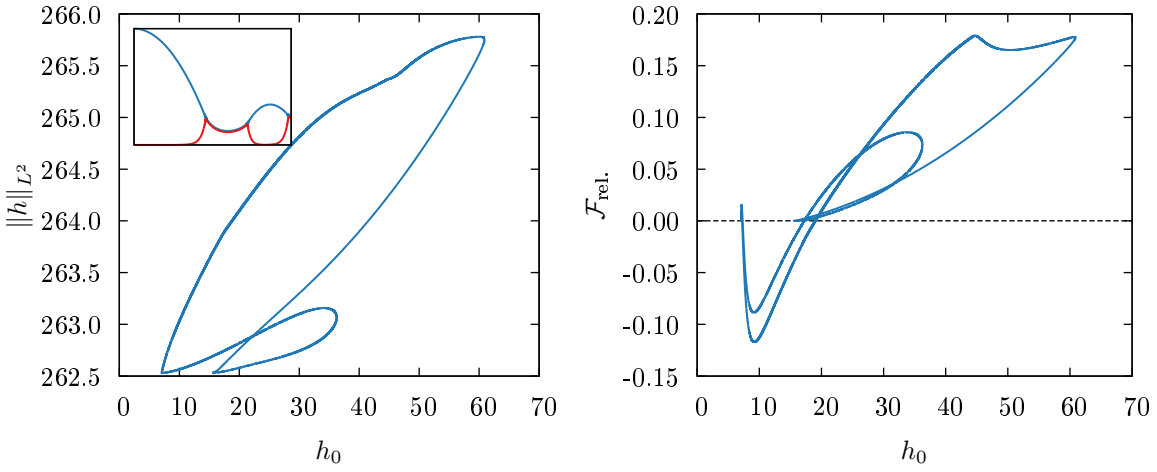

Figure 23: Left: L^2-norm depending on the mean height of the upper layer h_0. Right: Relativ free energy $\mathcal{F}_{\text{rel.}}$ depending on the mean height of the upper layer h_0. Both graphs show the behavior of the radial elastic model model for a drop number of $d_p = 1.5$. A solution for this drop number is shown in the small box inside the left graph.

effect on the L^2-norm plot in the mean height h_0 extension.

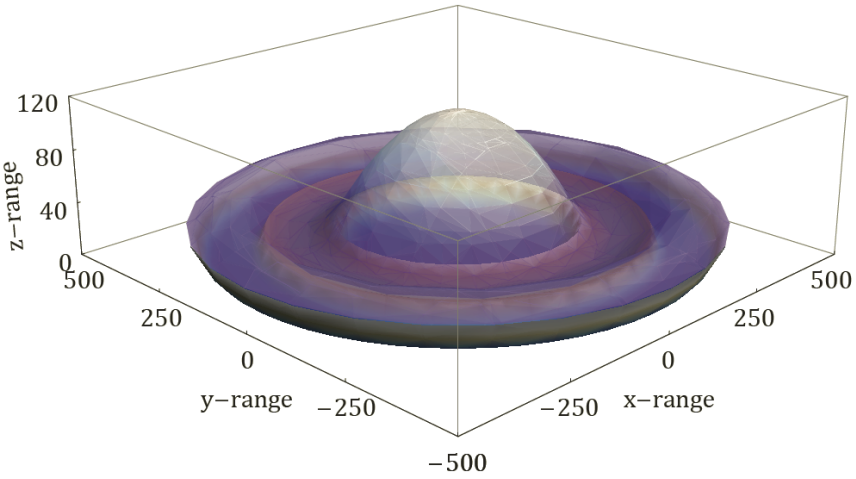

Figure 24: 3D plot of the radial symmetric solutions for $d_p = 1.5$. The domain size is $L = 500$, the ratio of interface tensions is $\sigma = 0.1$ and the vertical compression elasticity is $\kappa_v = 0.001$. This figure is produced with *Mathematica* using the function RevolutionPlot3D.

The solution that is depicted in figure (23) is again plotted in 3D with *Mathematica* to give a perspective view of its axisymmetric shape, see figure (24). It can be seen in figure (24) that the

outer liquid ridge with its corresponding elastic ridge is pinned to the boundary. Continuing the process of increasing the drop number in steps of full drops $d_p+ = 1.0$ the bifurcation and relative free energy diagram for a drop number of $d_p = 2.5$ is produced, see figure (25). As seen for the drop number $d_p = 1.5$ the stretching effect in the mean height h_0 also occur in the L^2-norm bifurcation diagram. In the upper right quadrant of the the free energy curve there are once again the artifacts of the small domain. The outer rings formed for higher drop numbers $d_p \geq 1.5$ are also always

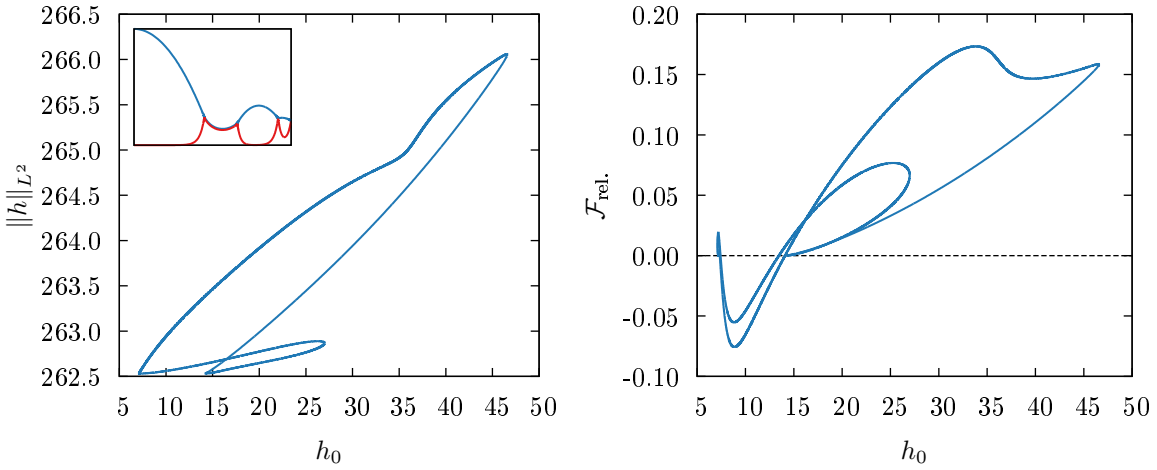

Figure 25: Left: L^2-norm depending on the mean height of the upper layer h_0. Right: Relativ free energy $\mathcal{F}_{\text{rel.}}$ depending on the mean height of the upper layer h_0. Both graphs show the behavior of the radial elastic model model for a drop number of $d_p = 2.5$. A solution for this drop number is shown in the small box inside the left graph.

pinned to the boundary. This seems to be a feature of the system and in this work no solutions with rings in the free space between the drop and the boundary without touching it could be produced. To make this even more plastic the solution is again represented as a surface plot with *Mathematica*, see figure (26). For a domain size of $L = 2000$ the bifurcation diagrams look completely different because the solution has more space to fill. There is also the possibility to have a higher drop number d_p as stable solutions. The following figure (27) shows the bifurcation diagram as well as the corresponding relative free energy diagram for a drop number of $d_p = 1.5$. The diagrams of the domain size $L = 500$ all showed artifacts due to constriction effects. Therefore, the domain size is increased to $L = 2000$ and the results are reproduced. The L^2-norm in the bifurcation diagram for this larger domain size envelopes a larger area for a drop number of $d_p = 1.5$ than the one for $L = 500$. Moreover, the energy diagram that is shown in the right graph changes its form completely.

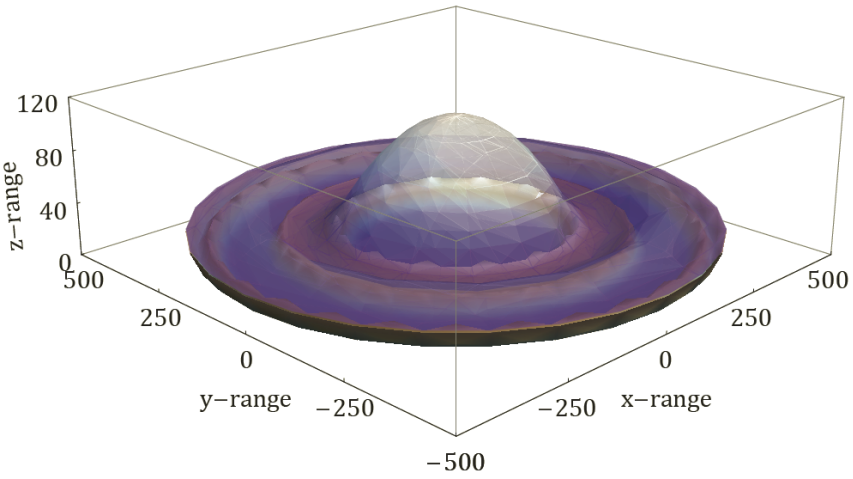

Figure 26: 3D plot of the radial symmetric solutions for $d_p = 2.5$. The domain size is $L = 500$, the ratio of interface tensions is $\sigma = 0.1$ and the vertical compression elasticity is $\kappa_v = 0.001$. There are two outer rings visible and the inner drop has shrinked in size. Also, the attentive reader could have noticed that all rings are pinned to the simulation boundary. This figure is produced with *Mathematica* using the function RevolutionPlot3D.

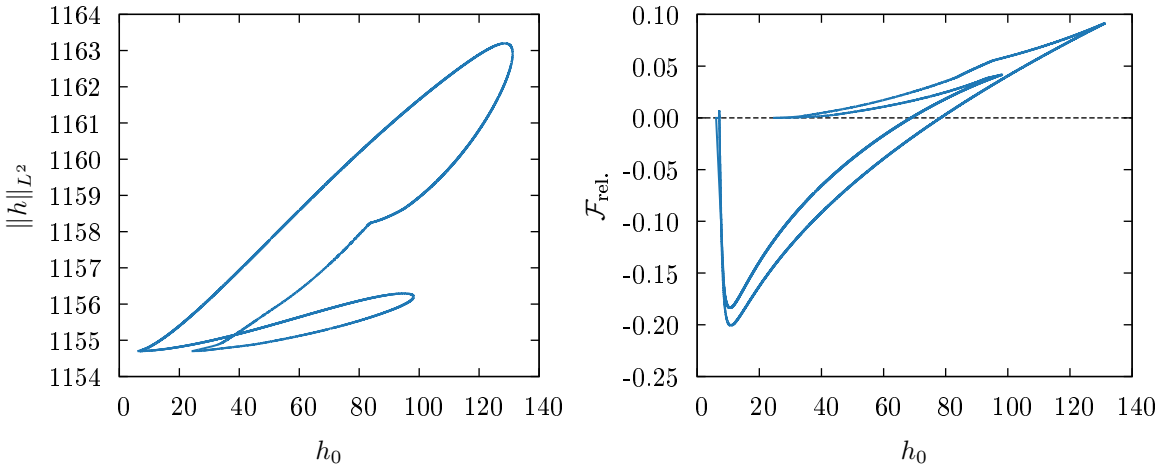

Figure 27: Left: L^2-norm depending on the mean height of the upper layer h_0. Right: Relativ free energy $\mathcal{F}_{\text{rel.}}$ depending on the mean height of the upper layer h_0. Both graphs show the behavior of the radial elastic model model for a drop number of $d_p = 1.5$, but on a domain size of $L = 2000$.

To specify, the main structure of two branches under the relative free energy of the flat film that is indicated by the dashed zero line stays the same. Nevertheless the form of the part with an energy

over that of a flat film changes completely. The branches do not intersect anymore and the loop that connects both branches for the lower domain size is now straightened out. On top of that, there is also a zero solution at a mean height of the upper layer of $h_0 \approx 23$, this is where the drop in the center changes to a hole. In the figure (28) the bifurcation and relative free energy diagram

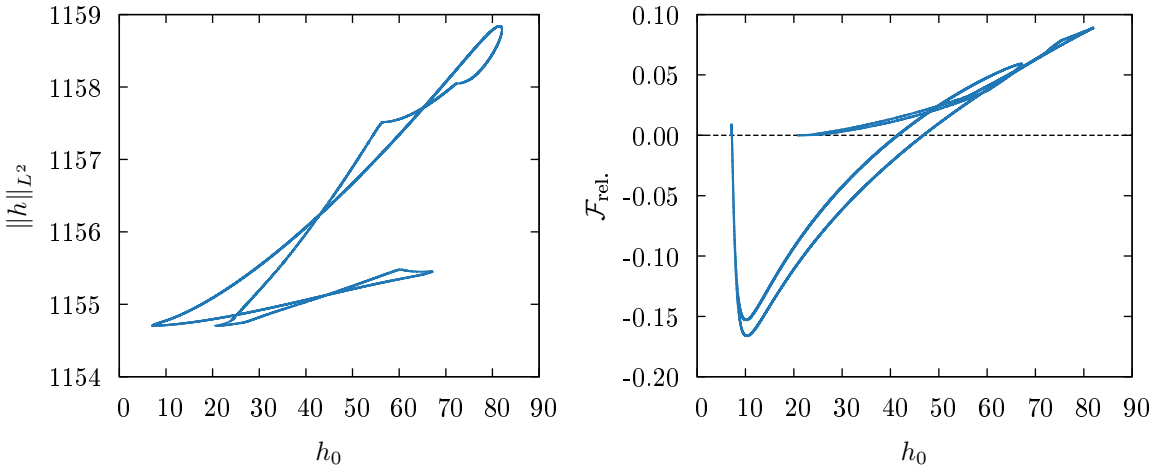

Figure 28: Left: L^2-norm depending on the mean height of the upper layer h_0. Right: Relativ free energy $\mathcal{F}_{\text{rel.}}$ depending on the mean height of the upper layer h_0. Both graphs show the behavior of the radial elastic model model for a drop number of $d_p = 2.5$, but on a domain size of $L = 2000$.

for a drop number of $d_p = 2.5$ is shown on the larger domain of $L = 2000$. The corresponding solutions for these diagrams are shown in the appendix C. The diagrams look completely different to anything seen before in this work especially the L^2-norm bifurcation diagram has 4 crossings of the branches. Besides, the curve in general is compressed in the L^2-norm and in the mean liquid film height h_0 values compared to a lower drop number. This is expected as it can also be seen for a radial thin film equation without an elastic substrate (see appendix B). Comparing the solutions from the same qualitative positions (see figure(29)) in the curves of the same drop number $d_p = 2.5$ but on domain sizes $L = 500$ and $L = 2000$ one can again see that the drop number is too high for the lower domain size. Therefore, the fact that the bifurcation diagram changed seems to indicate that the bifurcation diagram for the larger domain size is closer to the real, free bifurcation diagram without strong boundary effects. The energy diagram above the dashed zero line of relative free energy is characterized by a higher complexity than before with two loops and many crossings in which concerning free energy both solutions are possible. It should be noted that no conclusions to the stability of the solutions can be made from this plots. For higher drop number and larger

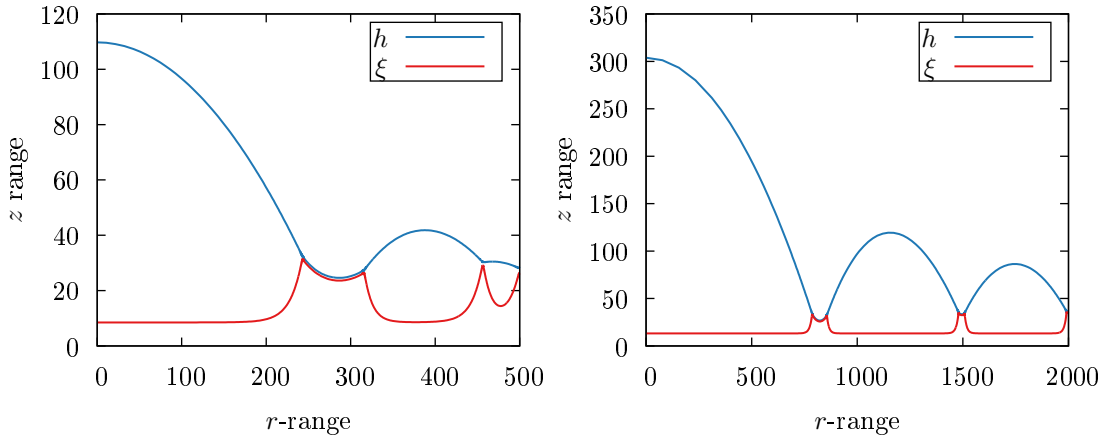

Figure 29: Comparing solutions of different domain sizes $L = 500$ (left) and $L = 2000$ (right) for a drop number of $d_p = 2.5$. The solutions chosen are the highest in the L^2-norm possible. It is obvious that the solution on the smaller domain size (left) is warped at the right boundary and therefore the domain is too small for it.

domain sizes an even greater complexity can be found.

6.2.1 Contact angle

The dependence of the contact angle θ on the softness parameter $\frac{\gamma_l}{\kappa_v R}$ is also interesting for this radial case. Comparing to the *Cartesian* elastic model there are a few new features. First of all, the contact angle θ_{lg} at the side of the drop is given by the maximum of the derivative of the liquid height profile $\frac{\mathrm{d}h(r)}{\mathrm{d}r}\Big|_{\max}$. The dependence on the softness parameter for a drop in the center and a domain size of $L = 500$ is shown in figure (30, left).

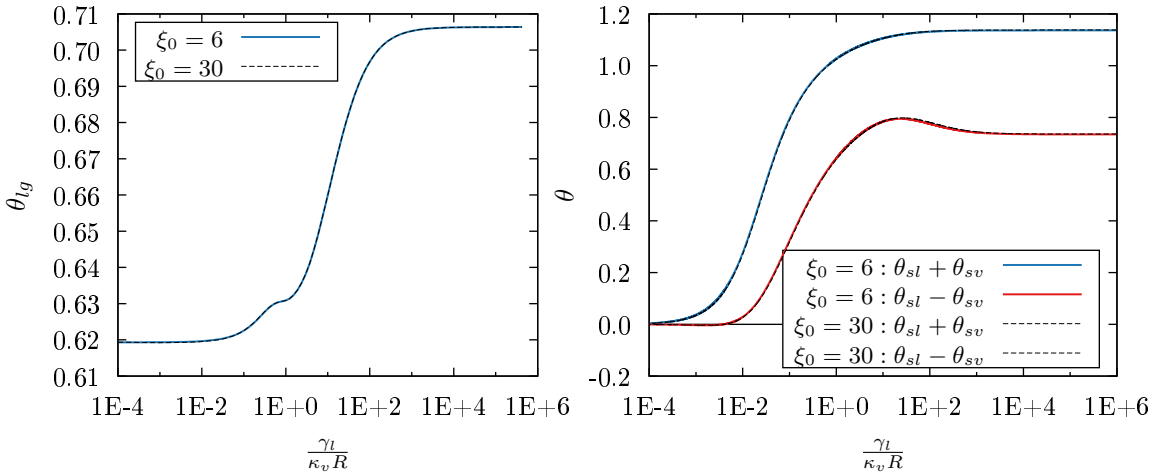

Figure 30: Left: θ_{lg} depending on the dimensionless quantity $\frac{\gamma_l}{\kappa_v R}$, wherein R is the radius of the drop. Right: θ_{sl} and θ_{sv} combined dependency on the same dimensionless quantity. Both plots are done with a ratio of interface tensions $\sigma = \frac{\gamma_l}{\gamma_s} = 0.1$ and on a domain size of $L = 500$.

One can identify the same constant plateaus in the limits of the softness parameter as in the *Cartesian* case. This time the angle is the liquid-gas angle θ_{lg} as shown in figure (5, (b)). For the limit of high vertical compression elasticity κ_v this angle goes to the angle on a hard substrate that is here given by $\theta_{lg,l} = 0.619$. The other side is given by the fluid-fluid limit and the angle goes to $\theta_{lg,r} = 0.707$. A new phenomenon for this radial case is given by the small bulb at the start of the increasing curve indicating that the liquid-gas angle θ_{lg} increases faster in the range around the softness parameter value of 0.1 than in the *Cartesian* case. As one could expect, this effect is also independent of the mean height of the elastic layer ξ_0, since the model does not consider interactions of the elastic layer with the rigid subsoil. In comparison to [27] the right plot in figure (30) shows the dependence of $\theta_{sl} \pm \theta_{sv}$ on the softness parameter $\frac{\gamma_l}{\kappa_v R}$. In this plot, there are two bulbs in the curve of $\theta_{sl} - \theta_{sv}$, the first one stretches the curve to the negative values at the start of the curve. This indicates that the solid-vapor angle θ_{sv} is larger than the solid-liquid angle θ_{sl} for a short interval of the softness parameter between 0.001 and 0.01. Before the curve saturates to the liquid limit there is a bulb of height 0.5 in θ in the positive direction (right) where the solid-vapor angle θ_{sv} decreases as the solid-liquid angle θ_{sl} increases. Again, the effects are independent of the mean height of the elastic layer ξ_0.

7 Time simulations with *DUNE*

Distributed and Unified Numerics Environment, or short *DUNE* is a free (GPL) modular library for solving partial differential equations with different grid-based methods like finite elements [2]. It is quite common in the numerical treatment of partial differential equations to use discretization algorithms, which transform the equations to a set of ordinary differential equations. In this work a conform finite element semi-discretization is used. The linear solver used by the code in this work is a biconjugated-stabilized-gradient (*BiCGSTAB*) method [46] combined with a iterative *Gauß-Seidel* relaxation method. The *BiCGSTAB* algorithm is considered fast and smoothly converging to produce a solution for nonsymmetric linear systems. Since all models in this work are also time dependent a Alexander-2-Parameter time stepper is used for the time integration. This is basically a diagonally implicit *Runge-Kutta* algorithm for stiff ordinary differential equations [1]. After each step the program can also use a standard *Newton* algorithm to ensure convergence. Mathematically, it is important to know how *Lebesque* and *Sobulev* spaces are defined to understand why a weak formulation of the equations to simulate is preferred by *DUNE*. A *Lebesque* space $L^p(\Omega)$ is a complete and normed vector space (*Banach* space) that is defined by:

$$L^p(\Omega) := \left\{ u : \Omega \mapsto \mathbb{R} \middle| \|u\|_{L^p(\Omega)} = \left(\int_\Omega |u|^p \, \mathrm{d}x \right)^{\frac{1}{p}} < \infty \right\}. \tag{7.1}$$

Here, $\Omega \subset \mathbb{R}^n$ is the domain, in *Euclidean* space that has a sufficiently regular boundary, of the model of n equations. Such a domain is called *Lipschitz* domain and is important for the use of *Sobulev* spaces to describe partial differential equations which is our aim. For our purposes it is sufficient to use the specific space $L^2(\Omega)$ in which the scalar product $\langle ., . \rangle = L^2(\Omega) \times L^2(\Omega) \mapsto \mathbb{R}$ is given by the simple integral:

$$\langle u, v \rangle := \int_\Omega uv \, \mathrm{d}x. \tag{7.2}$$

We now define test functions $\varphi := \{\Omega \mapsto \mathbb{R} \in \mathcal{C}_C^\infty(\Omega)\}$, these are infinitely differentiable functions with compact support in Ω. Compactness is denoted by the C suffix and means that the functions vanish near the boundary $\delta\Omega$. We further assume that we can use integration by parts and such get the motivation for the usage of weak derivatives:

$$\int_\Omega u D^\alpha \varphi \, \mathrm{d}x = (-1)^{|\alpha|} \int_\omega D^\alpha u \varphi \, \mathrm{d}x. \tag{7.3}$$

The operator D^α is the so-called weak derivative operator that can be identified as the classical derivative for classical differentiable functions . The *Sobulev* space $W^{k,p}(\Omega)$ consists of all locally summable functions u such that the weak derivative $D^\alpha u$ exists in $L^p(\Omega)$ [12]. For our case the

restriction to $p = [1, \infty)$ is sufficient and for this the space is defined as:

$$\|u\|_{W^{k,p}(\Omega)} = \left(\sum_{|\alpha| \leq k} \int_\Omega |D^\alpha u|^p_{L^p(\Omega)} \, \mathrm{d}x \right)^{\frac{1}{p}}. \tag{7.4}$$

It is common practice to define the *Hilbert* space $H^k(\Omega) := W^{k,2}(\Omega)$. For our purposes $k = 1$ is the most used space in which the scalar product is given by [4]:

$$\langle u, v \rangle_{H^1(\Omega)} = \int_\Omega uv \, \mathrm{d}x + \int_\Omega \nabla u \cdot \nabla v \, \mathrm{d}x. \tag{7.5}$$

It is now helpful to give a short introduction to the finite element method. The main advantage of this method is that it can be used for all kinds of areas/volumes that can also be curvilinear. It is based on the fact that one can subdivide the domain, on which the calculations have to be performed, and then use a variation over the subdomains to find the solution $\mathbf{u}$ of the differential equation for each element. The main concept of finite elements is that the general solution is given by the sum over each element $i \in [1, n]$ with its specific ansatz function N_i:

$$\mathbf{u} = \sum_i N_i u_i. \tag{7.6}$$

The general form of such a concept is given by the action integral [18]:

$$\mathcal{S} = \underbrace{\int_\Omega I(\mathbf{u}, \mathbf{u}', \ldots) \, \mathrm{d}x}_{\text{interior}} + \underbrace{\int_{\delta\Omega} B(\mathbf{u}, \mathbf{u}', \ldots) \, \mathrm{d}x}_{\text{boundary}}. \tag{7.7}$$

If for each element the variation $\delta\mathcal{S}$ with respect to the individual u_i can be set to zero the equation is solved under the given boundary conditions. In the *DUNE* library a quadrangulation of the surface area Ω is used. Since the library can only process differential equations up to second order in the differential operators, transforming them into the weak formulation leaves us with only equations of first order in derivatives. In view of this, it is clear that the toolbox uses linear ansatz functions as more advanced functions also provide the information for higher order derivatives that is not needed. The quadrangulation of a 2D domain is shown in figure (31). The boundary variation can also be simplified for such a grid by just summing over the partial derivatives of the knot values a_j multiplied with their variations:

$$\delta\mathcal{S} = \sum_j \frac{\partial \mathcal{S}}{\partial a_j} \delta a_j = 0. \tag{7.8}$$

It is therefore import for the library to get as much information on the grid used as possible to make the computation as efficient as possible. There are many more important tricks on how to increase the efficiency and flexibility of the grid that are packed into the dune-grid module [2].

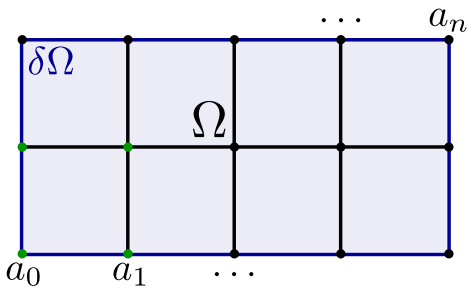

Figure 31: Sketch of the quadrangulation of a domain Ω with boundary $\delta\Omega$ and knot values a_j.

7.1 Two layers defined with relative thicknesses

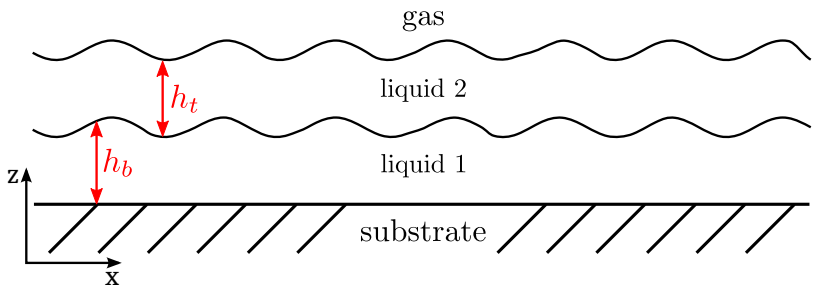

Figure 32: Sketch of the two-layer model with relative fields. That means, the thickness of the fields are defined to the next interface instead of to the base substrate.

The free energy of the relative defined two layer model in figure (32) is given by [35]:

$$\mathcal{F}[h_b, h_t] = \int_\Omega \left[\frac{\gamma_b}{2} \left(\nabla h_b\right)^2 + \frac{\gamma_t}{2} \left(\nabla (h_b + h_t)\right)^2 + f(h_t) \right] \mathrm{d}x. \tag{7.9}$$

Therefore, following equation (2.51) the time evolution is given by the following system of equations:

$$\frac{\partial h_b}{\partial t} = \nabla \left(Q_{bb} \nabla \frac{\delta \mathcal{F}}{\delta h_b} + Q_{bt} \nabla \frac{\delta \mathcal{F}}{\delta h_t} \right), \tag{7.10}$$

$$\frac{\partial h_t}{\partial t} = \nabla \left(Q_{tb} \nabla \frac{\delta \mathcal{F}}{\delta h_b} + Q_{tt} \nabla \frac{\delta \mathcal{F}}{\delta h_t} \right). \tag{7.11}$$

The symmetric mobility matrix Q_{ij} with $i, j \in \{t, b\}$ is for this case given by:

$$Q_{ij} = \frac{1}{6\mu_b} \begin{pmatrix} 2h_b^3 & 3h_b^2 h_t \\ 3h_b^2 h_t & 2\mu h_t^3 + 6h_b h_t^2 \end{pmatrix}, \tag{7.12}$$

wherein $\mu = \frac{\mu_t}{\mu_b}$. The local free energy function $f(h_t)$ that describes the interaction of the layers is as again defined as:

$$f(h_t) = \frac{1}{2h_t^2} - \frac{h_{pc}^3}{5h_t^5}. \tag{7.13}$$

Therefore after the using the functional derivatives the disjoining pressure $\Pi(h_t) = -\partial_{h_t} f(h_t)$ is given by:

$$\Pi(h_t) = \frac{1}{h_t^3}\left(1 - \left(\frac{h_{pc}}{h_t}\right)^3\right). \tag{7.14}$$

Performing again the functional derivatives, one gets [1]:

$$\frac{\delta \mathcal{F}}{\delta h_b} = -\gamma_b \triangle h_b - \gamma_t(\triangle h_b + \triangle h_t), \tag{7.15}$$

$$\frac{\delta \mathcal{F}}{\delta h_t} = -\gamma_t(\triangle h_b + \triangle h_t) + \Pi(h_t). \tag{7.16}$$

For the implementation in *DUNE*, the model may include at maximum second order derivatives and therefore it has to be transformed into a system of differential equations of second order.

$$\partial_t h_b = \nabla \cdot [Q_{bb}\nabla h_{bw} + Q_{bt}\nabla h_{tw}], \tag{7.17}$$

$$h_{bw} = -\gamma_b \triangle h_b - \gamma_t (\triangle h_b + \triangle h_t), \tag{7.18}$$

$$\partial_t h_t = \nabla \cdot [Q_{tb}\nabla h_{bw} + Q_{tt}\nabla h_{tw}], \tag{7.19}$$

$$h_{tw} = -\gamma_t (\triangle h_b + \triangle h_t) + \Pi(h_t). \tag{7.20}$$

The equations are defined on $\Omega \times \Sigma$, where $\Omega = [0, L_x] \times [0, L_y]$ is the spatial domain and $\Sigma = [0, T]$ the time interval $(L_x, L_y, T > 0)$. *Neumann* conditions are used as boundary conditions:

$$\nabla h_b \cdot n = \nabla h_t \cdot n = 0, \text{ auf } \delta\Omega \tag{7.21}$$

and the initial fields are given by:

$$h_b(\cdot, 0) = U_b(\cdot) \quad \text{und} \quad h_t(\cdot, 0) = U_t(\cdot). \tag{7.22}$$

Furthermore, the local operator of a *DUNE* program needs the weak formulation, therefore the equations are once again integrated over the domain. The fields h_b, h_{bw}, h_t, h_{tw} are elements of the *Lebesque* space $L^2(\Sigma; H^1(\Omega)$ and the test functions $\varphi_{hb}, \varphi_{hbw}, \varphi_{ht}, \varphi_{htw}$ are elements of the *Hilbert*

[1] Remark: The term

$$\mathcal{F}_{h_t} = \int_\Omega \frac{\gamma_t}{2} (\nabla(h_b + h_t))^2 \, \mathrm{d}x,$$

gives the same contribution for both *Fréchet* derivatives:

$$\frac{\delta \mathcal{F}_{h_t}}{\delta h_b} = \frac{\delta}{\delta h_b} \int_\Omega \frac{\gamma_t}{2} \left[(\nabla h_b)^2 + 2\nabla h_b \nabla h_t + (\nabla h_t)^2\right] \mathrm{d}x = -\frac{\gamma_t}{2} (2\triangle h_b + 2\triangle h_t) = -\gamma_t \triangle (h_b + h_t).$$

space $H^1(\Omega)$.

$$\int_\Omega \partial_t h_b \varphi_{hb}\,\mathrm{d}x + Q_{bb}\int_\Omega \nabla h_{bw}\cdot\nabla\varphi_{hb}\,\mathrm{d}x + Q_{bt}\int_\Omega \nabla h_{tw}\cdot\nabla\varphi_{hb}\,\mathrm{d}x = 0, \tag{7.23}$$

$$\gamma_b\int_\Omega \nabla h_b\cdot\nabla\varphi_{hbw}\,\mathrm{d}x + \gamma_t\int_\Omega (\nabla h_b+\nabla h_t)\cdot\nabla\varphi_{hbw}\,\mathrm{d}x - \int_\Omega h_{bw}\varphi_{hbw}\,\mathrm{d}x = 0, \tag{7.24}$$

$$\int_\Omega \partial_t h_t \varphi_{ht}\,\mathrm{d}x + Q_{tb}\int_\Omega \nabla h_{tw}\cdot\nabla\varphi_{ht}\,\mathrm{d}x + Q_{tt}\int_\Omega \nabla h_{tw}\cdot\nabla\varphi_{ht}\,\mathrm{d}x = 0, \tag{7.25}$$

$$\gamma_t\int_\Omega (\nabla h_b+\nabla h_t)\cdot\nabla\varphi_{htw}\,\mathrm{d}x + \int_\Omega (\Pi(h_t)-h_{tw})\varphi_{htw}\,\mathrm{d}x = 0. \tag{7.26}$$

This is the full system of equations that can be plugged into the local operator of the *DUNE* program. The solution of this two field model with parabular drops as initial conditions for the upper and lower field and different viscosities $\mu_t = 1$ and $\mu_b = 100$ are shown in figure (33). As one can see, the domain size is given by $L_x = 500$ and $L_y = 500$, also it is important to note that the field heights are scaled by a factor of 3.

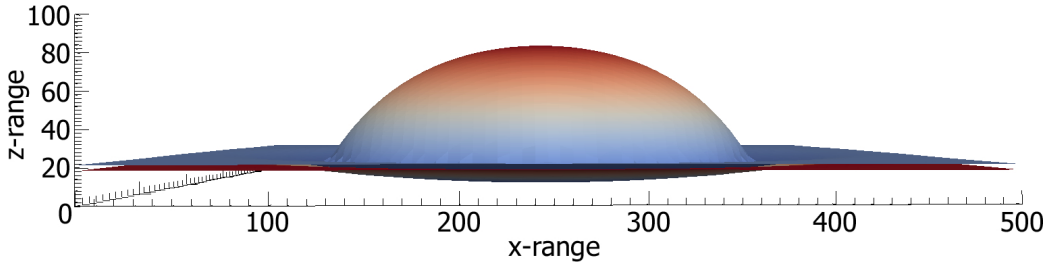

Figure 33: Drop solution of the two-layer model produced with *DUNE*. The lower field has a much higher viscosity $\mu_b = 100$ than the upper field $\mu_t = 1$, therefore the image does not show the final static state. It is important to note that the field heights are scaled by a factor of 3.

Because of the high viscosity of the lower field, the shape in the simulation frame has not converged to a static shape, therefore the upper drop has shrinked in size from the initial state and the lower inverse drop still has its initial shape.

7.2 Inclined upper layer

To tilt the upper layer, the equation for h_t transforms to:

$$\partial_t h_t = \nabla\cdot[Q_{tb}\nabla h_{bw} + Q_{tt}\nabla h_{tw}] + G_0\,\nabla\cdot Q_{tt}\,\alpha, \tag{7.27}$$

in which $G_0 = 0.001$ a scaling constant and $\boldsymbol{\alpha}$ is the inclination vector for a small angle $\tan(\alpha) \approx \alpha$ and an inclination only in x-direction it is given by:

$$\boldsymbol{\alpha} = \begin{pmatrix} \alpha \\ 0 \end{pmatrix}. \tag{7.28}$$

The additional term in the equation can be derived by a projection of the potential energy to the x and z axis and incorporating it into the system for small projection angles. This changes the equations in the weak formulation accordingly to:

$$\int_\Omega \partial_t h_t \varphi_{ht} \,\mathrm{d}x + Q_{tb} \int_\Omega \nabla h_{tw} \cdot \nabla \varphi_{ht} \,\mathrm{d}x + Q_{tt} \int_\Omega \nabla h_{tw} \cdot \nabla \varphi_{ht} \,\mathrm{d}x + G_0 \int_\Omega Q_{tt}\, \boldsymbol{\alpha} \cdot \nabla \varphi_{ht} \,\mathrm{d}x = 0. \tag{7.29}$$

Figure (34) shows solutions for different inclinations. The most interesting feature has been observed

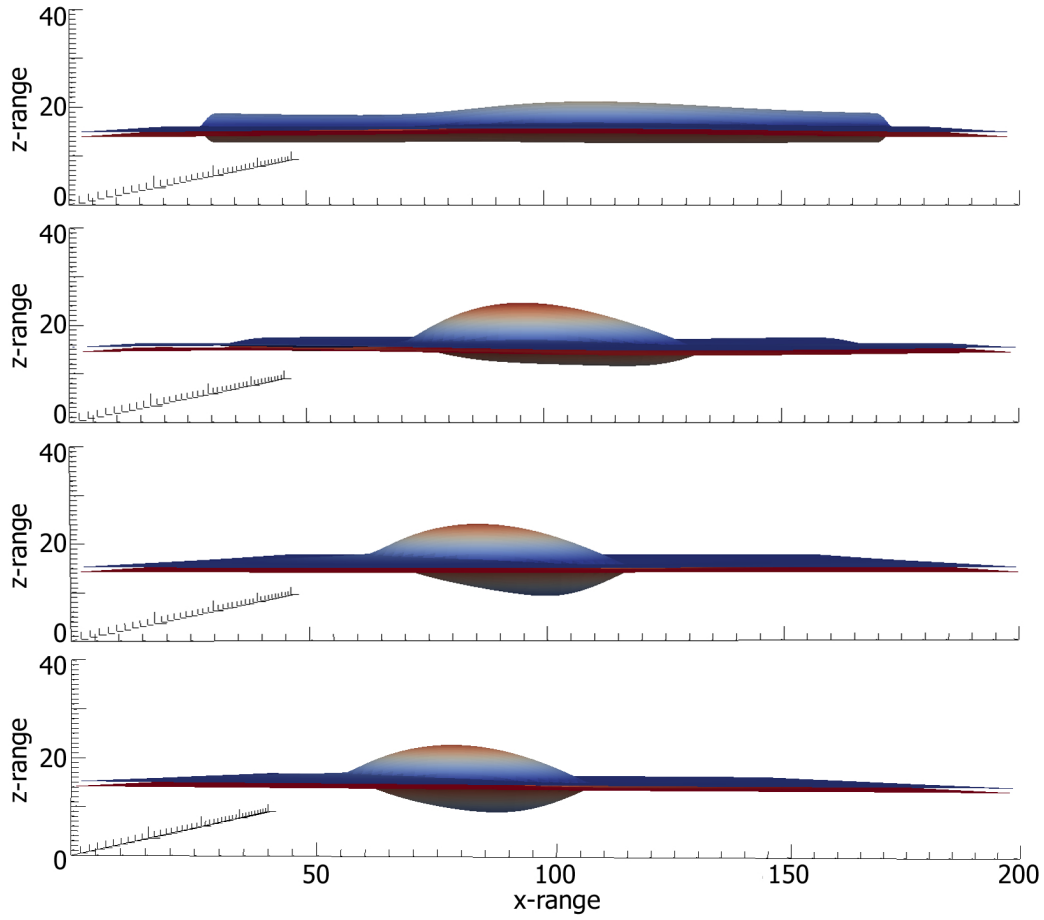

Figure 34: Solutions of the inclined two-layer model for different inclinations produced with *DUNE*. The inclinations from bottom to top are given by $\alpha = 0.25$, $\alpha = 0.50$, $\alpha = 1.00$ and $\alpha = 2.00$.

for an inclination of $\alpha = 2$ as in this simulation, before forming the ridge over the whole domain, a small drop has become detached from the moving initial drop solution. In all the other simulations the upper layer drop drags the anti drop form in the lower layer behind in a steady motion.

7.3 Simple elasticity with inclined upper layer

In this subsection, the inclined model (7.27) is extended with the simple elastic term known from previous sections. This changes the sub-equation for the lower elastic layer h_{bw} to:

$$h_{bw} = -\gamma_b \triangle h_b - \gamma_t \left(\triangle h_b + \triangle h_t\right) + \kappa_v (h_b - h_{b,0}). \tag{7.30}$$

The parameter κ_v is again the vertical compression elasticity and $h_{b,0}$ is the mean value of the lower field. As before, the weak formulation changes accordingly and the elastic term is included:

$$\gamma_b \int_\Omega \nabla h_b \cdot \nabla \varphi_{hbw} \,\mathrm{d}x + \gamma_t \int_\Omega (\nabla h_b + \nabla h_t) \cdot \nabla \varphi_{hbw} \,\mathrm{d}x + \int_\Omega \left(\kappa_v (h_b - h_{b,0}) - h_{bw}\right) \varphi_{hbw} \,\mathrm{d}x = 0. \tag{7.31}$$

Contrary from what is expected from the form of the solutions produced with continuation, the motion for a vertical compression elasticity of $\kappa_v \lessapprox 0.01$ is characterized by a high fluidity. Therefore, the vertical compression elasticity has been set to $\kappa_v = 0.1$ for the simulations as for lower values the elastic layer acts as a liquid and the material has problems forming the expected ridges at the contact line. The ridge in the bottom layer h_b for this choice of parameters on a domain of size $L = 500$ with a very low inclination is shown in figure (35).

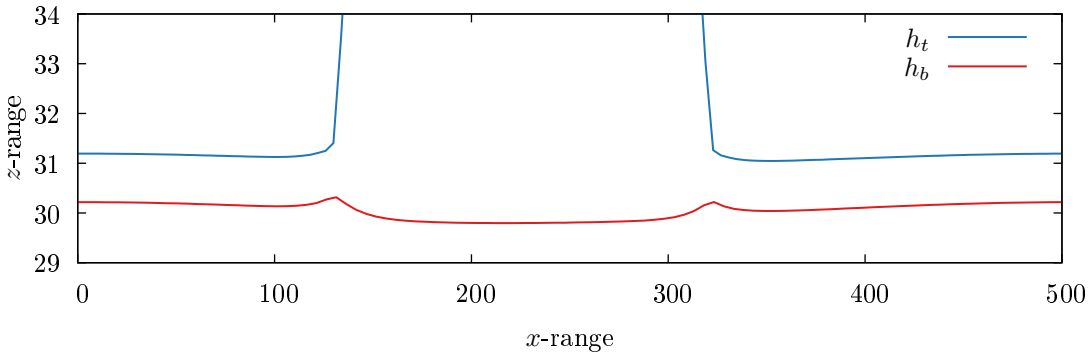

Figure 35: 2D Plot of an intersection through the drop zoomed in on the contact line. The vertical compression elasticity is $\kappa_v = 0.1$ and the domain size is $L = 500$.

The other important parameter in time simulations of this system is the viscosity of the layers μ_b and μ_t. To start looking for the expected stick-slip motion, approximate boundaries in which the

motion should occur are produced by a lot of simulations with bad resolutions ($N_x = N_y = 64$). All simulations are carried out with a domain size of $L = 500$ and the vertical compression elasticity has been set to either $\kappa_v = 0.1$ or $\kappa_v = 0.05$. Through the simulations in the different parameter ranges a restriction on the ratio of the viscosities to achieve a stick-slip motion of $\eta_{\text{st-sl}} = \frac{\mu_t}{\mu_b} \lessapprox \frac{1}{50}$ can be made. On top of that, the inclination angle of $\alpha < 0.01$ is too small to realize a stick-slip motion and an upper bound for the angle is given by $\alpha > 1.0$. In this range of the inclination angle α high resolution simulations ($N_x = N_y > 150$) have been concluded for values of α=0.01, 0.02, 0.03, 0.04, 0.05, 0.1, 0.2, 0.3, 0.4 and 0.5 and different values of the lower layer viscosities μ_b=50, 75, 100, 150, 200 and 500. The upper viscosity has been set to $\mu_t = 1$ as only the ratio is important for the interaction of the materials in the bilayer system. Since the program code is fully parallel, some of these simulations were carried out on the supercomputer *Palma* that allows to cover a large region of the parameter space in a short time span. Except from some curious cases in which the grid causes some kind of stick-slip motion that has nothing to do with the physical motion, there have been no clear signs of a stick-slip motion in all this simulations. Concerning this, a good explanation is that in this model only two time scales are present, one for the moving upper liquid given by the inclination α and one in the relaxation time of the lower layer. In the first experimental paper describing the stick-slip motion by Kajiya et al. [21] an advancing contact line is created by an inflow of liquid volume through a needle to inflate the drop. As the volume increases with this flow the contact line of the 3D drop advances, but this motion gets increasingly slower as more volume is needed to move the contact line in the same speed. Hence, the third time scale is introduced by the decreasing speed of the contact line. In their later experimental paper explaining the motion of a receding contact line, a third time scale can be identified by the dragging speed of the subsoil plate [20]. These considerations suggest that, to see a stick-slip motion, the model may need to be extended with a third time scale.

8 Discussion of the results

In conclusion, this work has, for the first time, introduced an elastic substrate in the theoretical description using the thin film equation. To achieve this goal, the theoretical background for (visco)elasticity has been put together in a coherent form and is shown in the first part of this thesis. Thereby, a simple model for a liquid on an elastic layer has been derived from the full viscoelastic description of the substrate material. On top of that, the toolbox *auto07p* using the technique of continuation in pseudoarclength has been applied to find static solutions of this elastic model. It could be shown that the model reproduces all important features known for drops on elastic substrates, like the ridge forming in the elastic layer at the contact line of the drop. Moreover, this static model gives a validity range for the time simulations by providing the information on how to choose the parameters, like the vertical compression elasticity κ_v. Since drops without external forces have an axisymmetrical shape, the equations have been transformed to cylindrical symmetry to form a radial elastic model. This radial model reproduced one of the main results of Lubbers et al. [27] figure 4 in the dependence of the contact angles on the softness parameter $\frac{\gamma_l}{\kappa_v R}$. There is also a new feature, as new bulges at the start of the increasing curve and at the end of the increase have been found. This new feature is also independent of the thickness of the lower layer as the model contains no interactions with the rigid subsoil. In addition, it is shown that the bifurcation structure depends strongly on the kind of solution in consideration that is in this work characterized by the drop number d_p. Also, it has been demonstrated that the diagrams for the L^2-norm and the relative free energy $\mathcal{F}_{\text{rel.}}$ change drastic if the domain size is too small for the solutions considered. The L^2-norm bifurcation diagrams tend to stretch in the mean height h_0 direction and the upper right quadrant of the free energy plot changes completely due to boundary effects. At last, a technique to switch between the solution branches for different drop numbers d_p has been introduced and applied in the radial elastic model as well as in the standard radial drop model (appendix B).

On the subject of time simulations with *DUNE*, the *Cartesian* model has been redefined to relative fields heights of the layers h_b and h_t. Likewise, the model has been set to the weak formulation and solutions for different inclinations of the upper liquid layer have been produced in preparation for the simulation of the probable stick-slip motion. In the end, the simple elasticity term has been introduced to the model to enable the emergence of ridges in the lower layer. It has been found that the vertical compression elasticity has to be larger than $\kappa_v > 0.01$ for the lower layer to form ridges and be sufficiently firm to enable a stable motion. Besides, a range for the possible occurrence of stick-slip motion has been set and it has been identified that a third time scale may be introduced to see the motion.

This work enables a lot of future research in the scope of elastic layers in the frame of coupled thin film equations. Some remarks on the future of this topic are given in the outlook.

8.1 Outlook

There are multiple possibilities to work further on the model produced in this thesis. An easy extension is to consider higher drop number solutions and larger domains to increase the complexity in bifurcation diagrams. In addition, for all the models the interactions with the rigid substrate under the elastic layer are neglected as they are proposed to be in the thick film limit. Following this thought process it could be interesting to revisit the models with interactions between the elastic layer and the rigid substrate. On top of that, there is also the possibility to introduce prestructures under each layer to tune the position of the drops. With a prestructure in the radial elastic model it could be possible to produce solutions in which the rings can be fixed in the intermediate region between the central drop and the boundary. If a stick-slip motion can be found in future time simulations it should also be possible to do an advanced stability analysis to describe the time periodic, reoccurring states. The most important advance would be to construct a fully viscoelastic multi layer model in the thin film formalism. At the current understanding it is not clear if such a full model exists as it is not clear if viscoelastic behavior can be put to a gradient structure and therefore in the form of a thin film equation. Nevertheless, in the process of working on this topic together with Dr. Stefan Karpitschka and Prof. Jacco Snoeijer at the University of Twente, Enschede the following equation for a time dependent viscoelastic bottom layer has been proposed:

$$\xi(x,t) = \int_{-\infty}^{t} \mathrm{d}t' \, \Phi(t-t') \left[\frac{\mathrm{d}}{\mathrm{d}t'} \left(\frac{\delta F}{\delta \xi(x,t)} \right) \right]. \tag{8.1}$$

For this equation, the derivation of the positive semi-definiteness of the mobility matrix M_{ij} can be redone analogue to the standard way:

$$\partial_t \Psi_i = \int_{-\infty}^{\infty} \theta(t-t') \nabla \cdot \left[M_{ij}(t-t') \left(\nabla \left. \frac{\delta F}{\delta \Psi_i(x,t)} \right|_{t'} \right) \right] \mathrm{d}t' \tag{8.2}$$

$$\frac{\mathrm{d}F}{\mathrm{d}t} = \int_{-\infty}^{\infty} \int_{-\infty}^{\infty} \left(\left. \frac{\delta F}{\delta \Psi_j(x,t)} \right|_{t} \right) \theta(t-t') \nabla \cdot \left[M_{ij}(t-t') \left(\nabla \left. \frac{\delta F}{\delta \Psi_i(x,t)} \right|_{t'} \right) \right] \mathrm{d}x \mathrm{d}t' \tag{8.3}$$

$$= \int_{-\infty}^{\infty} \int_{-\infty}^{\infty} \left(\nabla \left. \frac{\delta F}{\delta \Psi_j(x,t)} \right|_{t} \right) \theta(t-t') M_{ij}(t-t') \left(\nabla \left. \frac{\delta F}{\delta \Psi_i(x,t)} \right|_{t'} \right) \mathrm{d}x \mathrm{d}t' \tag{8.4}$$

The minimal condition for this to hold is that $M^*_{ij}(t-t') = \theta(t-t') M_{ij}(t-t')$ is semi-positive definite $\forall\ t' \leq t$, with $\theta(t)$ being the usual *Heaviside* step function. It should be stressed, that the equation (8.1) does currently not follow from any derivation, but instead is just proposed to be consistent with the gradient form of the thin film equation.

9 Bibliography

[1] Alexander, R. (1977). Diagonally implicit runge-kutta methods for stiff o.d.e.'s. SIAM Journal on Numerical Analysis, 14(6):pp. 1006–1021.

[2] Bastian, P., Blatt, M., Dedner, A., Engwer, C., Fahlke, J., Gräser, C., Klöfkorn, R., Nolte, M., Ohlberger, M., and Sander, O. (2015). Dune - distributed and unified numerics environment. Web page.

[3] Böhnke, F. (1999). Finite Elemente Analysen zur Berechnung der Signalverarbeitung in der Cochlea. Habilitationsschrift, Technische Universität Ilmenau.

[4] Bongers, J. (2015). Anwendung der finite-elemente-methode auf ein cahn-hilliard-modell für langmuir-blodgett-transfer. master thesis.

[5] Brady, J. and Bossis, G. (1988). Stokesian dynamics. Annual Review of Fluid Mechanics, 20:111–157.

[6] Brinson, H. F. and Brinson, L. C. (2008). Polymer Engineering Science and Viscoelasticity. Springer-Verlag.

[7] Bronstein, I. N., Semendjajew, K. A., Musiol, G., and Mühlig, H. (2008). Taschenbuch der Mathematik (german). Harri Deutsch Verlag, 7 edition.

[8] de Gennes, P., Brochard-Wyart, F., and Quere, D. (2004). Capillarity and Wetting Phenomena: Drops, Bubbles, Pearls, Waves. Springer.

[9] Doedel, E. J. (2010). Numerical analysis of nonlinear equations. Lecture Notes.

[10] Doedel, E. J., Champneys, A. R., Dercole, F., Fairgrieve, T., Kuznetsov, Y., Oldeman, B., Paffenroth, R., Sandstede, B., Wang, X., and Zhang, C. (2008). Auto-07p: Continuation and bifurcation software for ordinary differential equations. Webpage.

[11] Doi, M. (2011). Onsager's variational principle in soft matter. Journal of Physics: Condensed Matter, 23(28):284118.

[12] Ewans, L. C. (1998). Partial Differential Equations (Graduate Studies in Mathematics), volume 19. Oxford University Press, Inc. ISBN-10: 0821807722 ISBN-13: 978-0821807729.

[13] Extrand, C. and Kumagai, Y. (1996). Contact angles and hysteresis on soft surfaces. Journal of Colloid and Interface Science, 184(1):191 – 200.

[14] Ferry, J. D. (1980). Viscoelastic properties of polymers. John Wiley & Sons, first edition.

[15] Fick, A. (1995). On liquid diffusion. Journal of Membrane Science, 100(1):33 – 38. The early history of membrane science selected papers celebrating vol. 100.

[16] Galvagno, M., Tseluiko, D., Lopez, H., and Thiele, U. (2014). Continuous and discontinuous dynamic unbinding transitions in drawn film flow. Phys. Rev. Lett., 112:137803.

[17] Glasner, K. B. and Witelski, T. P. (2003). Coarsening dynamics of dewetting films. Phys. Rev. E, 67:016302.

[18] Hansen, U. (2013-2014). Fluiddynamik und numerische simulationen. Lecture Notes.

[19] Jerison, E. R., Xu, Y., Wilen, L. A., and Dufresne, E. R. (2011). Deformation of an elastic substrate by a three-phase contact line. Phys. Rev. Lett., 106:186103.

[20] Kajiya, T., Brunet, P., Royon, L., Daerr, A., Receveur, M., and Limat, L. (2014). A liquid contact line receding on a soft gel surface: dip-coating geometry investigation. Soft Matter, 10:8888–8895.

[21] Kajiya, T., Daerr, A., Narita, T., Royon, L., Lequeux, F., and Limat, L. (2013). Advancing liquid contact line on visco-elastic gel substrates: stick-slip vs. continuous motions. Soft Matter, 9:454–461.

[22] Karpitschka, S., Das, S., Andreotti, B., and Snoeijer, J. (2014). Dynamic contact angle of a soft solid. (Preprint).

[23] Kuznetsov, Y. A. (1998). Elements of Applied Bifurcation Theory, volume 112 of Applied Mathematical Sciences. Springer, second edition. Editors: Marsden, J. E. and Sirovich, L.

[24] Landau, L. and Lifshitz, E. (2013). Statistical Physics. Number 5 in Course of Theoretical Physics. Elsevier Science.

[25] Landau, L., Pitaevskii, L., Kosevich, A., and Lifshitz, E. (2012). Theory of Elasticity. Number 7 in Course of Theoretical Physics. Elsevier Science.

[26] Larson, R. G. (1999). The Structure and Rheology of Complex Fluids. Oxford University Press, Inc.

[27] Lubbers, L., Weijs, J., Botto, L., Das, S., Andreotti, B., and Snoeijer, J. (2014). Drops on soft solids: free energy and double transition of contact angles. Journal of Fluid Mechanics, 747.

[28] Matar, O., Gkanis, V., and Kumar, S. (2005). Nonlinear evolution of thin liquid films dewetting near soft elastomeric layers. J. Colloid Interface Sci., 286:319–332.

[29] Milner, S. T., Witten, T. A., and Cates, M. E. (1988). Theory of the grafted polymer brush. Macromolecules, 21(8):2610–2619.

[30] Onsager, L. (1931a). Reciprocal relations in irreversible processes. i. Phys. Rev., 37:405–426.

[31] Onsager, L. (1931b). Reciprocal relations in irreversible processes. ii. Phys. Rev., 38:2265–2279.

[32] Oron, A., Davis, S. H., and Bankoff, S. G. (1997). Long-scale evolution of thin liquid films. Rev. Mod. Phys., 69:931–980.

[33] Pismen, L. M. (2001). Nonlocal diffuse interface theory of thin films and the moving contact line. Phys. Rev. E, 64.

[34] Pismen, L. M. and Thiele, U. (2006). Asymptotic theory for a moving droplet driven by a wettability gradient. Physics of Fluids (1994-present), 18(4):–.

[35] Pototsky, A., Bestehorn, M., Merkt, D., and Thiele, U. (2005). Morphology changes in the evolution of liquid two-layer films. The Journal of Chemical Physics, 122(22):–.

[36] Reynolds, O. (1886). On the theory of lubrication and its application to mr. beauchamp tower's experiments, including an experimental determination of the viscosity of olive oil. Philosophical Transactions of the Royal Society of London (1776-1886), 177:157–234.

[37] Roman, B. and Bico, J. (2010). Elasto-capillarity: deforming an elastic structure with a liquid droplet. Journal of Physics: Condensed Matter, 22(49):493101.

[38] Rowlinson, J. and Widom, B. (2002). Molecular Theory of Capillarity. Dover books on chemistry. Dover Publications.

[39] Sadd, M. (2010). Elasticity: Theory, Applications, and Numerics. Elsevier Science.

[40] Sharma, A. and Ruckenstein, E. (1985). Mechanism of tear film rupture and formation of dry spots on cornea. Journal of colloid and interface science, 106(1):12–27.

[41] Skotheim, J. M. and Mahadevan, L. (2005). Soft lubrication: The elastohydrodynamics of nonconforming and conforming contacts. Physics of Fluids, 17(9):–.

[42] Thiele, U. (2010). Thin film evolution equations from (evaporating) dewetting liquid layers to epitaxial growth. Journal of Physics: Condensed Matter, 22(8):084019.

[43] Thiele, U. (2011). Note on thin film equations for solutions and suspensions. The European Physical Journal Special Topics, 197(1):213–220.

[44] Thiele, U. (2014). Structure formation in soft matter systems. Lecture Notes.

[45] Thiele, U., Brusch, L., Bestehorn, M., and Bär, M. (2003). Modelling thin-film dewetting on structured substrates and templates: Bifurcation analysis and numerical simulations. The European Physical Journal E, 11(3):255–271.

[46] van der Vorst, H. A. (1992). Bi-cgstab: A fast and smoothly converging variant of bi-cg for the solution of nonsymmetric linear systems. SIAM Journal on Scientific and Statistical Computing, 13(2):631–644.

[47] Watson, G. N. (1922). A Treatise on the Theory of Bessel Functions. Cambridge University Press.

[48] Weijs, J., Andreotti, B., and Snoeijer, J. (2013). Elasto-capillarity at the nanoscale: on the coupling between elasticity and surface energy in soft solids. Soft Matter, 9:8494–8503.

[49] Wilczek, M., Tewes, W. B.H., Gurevich, S. V., Köpf, M. H., Chi, L. F., and Thiele, U. (2015). Modelling pattern formation in dip-coating experiments. Math. Model. Nat. Phenom., 10(4):44–60.

[50] Xu, Y., Engl, W. C., Jerison, E. R., Wallenstein, K. J., Hyland, C., Wilen, L. A., and Dufresne, E. R. (2010). Imaging in-plane and normal stresses near an interface crack using traction force microscopy (supplement material). Proceedings of the National Academy of Sciences, 107(34):14964–14967.

[51] Zwanzig, R. (1961). Memory effects in irreversible thermodynamics. Phys. Rev., 124:983–992.

List of Figures

List of Tables

10 Acknowledgments

I thank: My supervisor Prof. Dr. Uwe Thiele for his motivation, immense knowledge and giving me the opportunity to work on this topic.
Dr. Svetlana Gurevich amongst many other things for agreeing to be second referee for this work.
Walter Tewes, Felix Tabbert and Sebastian Engelnkemper for the nice atmosphere in the office.
Jan Bongers for his *DUNE* tutorial and Markus Wilczek for his tips and codes for *DUNE*.
Prof. Dr. Jacco Snoeijer and Dr. Stefan Karpitschka from University Twente in Enschede for their time and helping me understanding viscoelasticity.

My gratitude also goes to my best friend Semir Vrana for prove reading this document and helping with motivation throughout my whole university career.
Furthermore, I am thankful to my family and in particular my parents Josef and Felicitas for their emotional and financial support.

In the end, I am grateful to Martina for accompanying me through good and bad times and her understanding of the time pressure of an aspiring physicist.

11 Appendix

A Nondimensionalization of the *Navier-Stokes* equation

$$
\begin{aligned}
\text{r:}\quad \frac{\epsilon u_0^2}{l}\frac{\partial u_R}{\partial T}+\frac{\epsilon u_0^2}{l}u_R\frac{\partial u_R}{\partial R}+\frac{\epsilon u_0^2}{l}u_Z\frac{\partial u_R}{\partial Z} &= -\frac{\nu u_0}{l^2}\frac{\partial P}{\partial R}+\frac{\nu u_0}{l^2}\left(\epsilon^2\frac{\partial^2 u_R}{\partial R^2}+\epsilon^2\frac{1}{R}\frac{\partial u_R}{\partial R}+\frac{\partial^2 u_R}{\partial Z^2}-\epsilon^2\frac{u_R}{R^2}\right)-\frac{\nu u_0}{l^2}\frac{\partial \Phi}{\partial R},\\
\frac{\epsilon u_0^2}{l}\left(\frac{\partial u_R}{\partial T}+u_R\frac{\partial u_R}{\partial R}+u_Z\frac{\partial u_R}{\partial Z}\right) &= -\frac{u_0^2}{l\mathrm{Re}}\frac{\partial P}{\partial R}+\frac{u_0^2}{l\mathrm{Re}}\left(\epsilon^2\frac{\partial^2 u_R}{\partial R^2}+\epsilon^2\frac{1}{R}\frac{\partial u_R}{\partial R}+\frac{\partial^2 u_R}{\partial Z^2}-\epsilon^2\frac{u_R}{R^2}\right)-\frac{u_0^2}{l\mathrm{Re}}\frac{\partial \Phi}{\partial R},\\
\epsilon\mathrm{Re}\left(\frac{\partial u_R}{\partial T}+u_R\frac{\partial u_R}{\partial R}+u_Z\frac{\partial u_R}{\partial Z}\right) &= -\frac{\partial P}{\partial R}+\frac{\partial^2 u_R}{\partial Z^2}+\epsilon^2\left(\frac{\partial^2 u_R}{\partial R^2}+\frac{1}{R}\frac{\partial u_R}{\partial R}-\frac{u_R}{R^2}\right)-\frac{\partial \Phi}{\partial R}.\\
\text{z:}\quad \frac{\epsilon^2 u_0^2}{l}\frac{\partial u_Z}{\partial T}+\frac{\epsilon^2 u_0^2}{l}u_R\frac{\partial u_Z}{\partial R}+\frac{\epsilon^2 u_0^2}{l}\frac{\partial u_Z}{\partial Z} &= -\frac{\nu u_0}{\epsilon l^2}\frac{\partial P}{\partial Z}+\frac{\nu u_0}{l^2}\left(\epsilon^3\frac{\partial^2 u_Z}{\partial R^2}+\epsilon^3\frac{1}{R}\frac{\partial u_Z}{\partial R}+\epsilon\frac{\partial^2 u_Z}{\partial Z^2}\right)-\frac{\nu u_0}{\epsilon l^2}\frac{\partial \Phi}{\partial Z},\\
\frac{\epsilon^2 u_0^2}{l}\left(\frac{\partial u_Z}{\partial T}+u_R\frac{\partial u_Z}{\partial R}+\frac{\partial u_Z}{\partial Z}\right) &= -\frac{u_0^2}{\epsilon l\mathrm{Re}}\frac{\partial P}{\partial Z}+\frac{u_0^2}{l\mathrm{Re}}\left(\epsilon^3\frac{\partial^2 u_Z}{\partial R^2}+\epsilon^3\frac{1}{R}\frac{\partial u_Z}{\partial R}+\epsilon\frac{\partial^2 u_Z}{\partial Z^2}\right)-\frac{u_0^2}{\epsilon l\mathrm{Re}}\frac{\partial \Phi}{\partial Z},\\
\epsilon^3\mathrm{Re}\left(\frac{\partial u_Z}{\partial T}+u_R\frac{\partial u_Z}{\partial R}+\frac{\partial u_Z}{\partial Z}\right) &= -\frac{\partial P}{\partial Z}+\epsilon^4\left(\frac{\partial^2 u_Z}{\partial R^2}+\frac{1}{R}\frac{\partial u_Z}{\partial R}\right)+\epsilon^2\frac{\partial^2 u_Z}{\partial Z^2}-\frac{\partial \Phi}{\partial Z},\\
\text{inc. cond.:}\quad \frac{\epsilon u_0}{l}\frac{1}{R}u_R+\frac{\epsilon u_0}{l}\frac{\partial u_R}{\partial R}+\frac{\epsilon u_0}{l}\frac{\partial u_Z}{\partial Z} &= 0,\\
\frac{1}{R}u_R+\frac{\partial u_R}{\partial R}+\frac{\partial u_Z}{\partial Z} &= 0.
\end{aligned}
$$

B Results: Radial thin film equation

In preparation of the radial elastic model the standard thin film equation has to be transformed to cylindrical coordinates. The derivation of this can be seen in subsection (2.2). One again has to set this equation to a set of equations of order one in derivatives for the use in *auto07p*. Since this is just the appendix and the whole procedure is the same as in the subsection of the radial elastic model (6.2) the showing of direct results should suffice. In figure (36) the bifurcation diagram of the model for different drop numbers d_p is shown. There is a maximum drop number that can be stable in the domain and the stability criterion following from linear stability is given by:

$$L_c = \frac{2\pi}{\sqrt{-\mathrm{d}_{hh} f(h)|_{h_0}}}. \tag{2.1}$$

For $h_0 = 3$ the critical length is given by $L_c = \frac{54}{5}\pi \approx 34$ and the domain size for this figure is $L = 100$, so the maximum stable drop numbers is $d_p = 1.5$. Therefore, it should be clear why the L^2-norm for a drop number of $d_p = 2.0$ increases again after decreasing before for increasing drop numbers in figure (36).

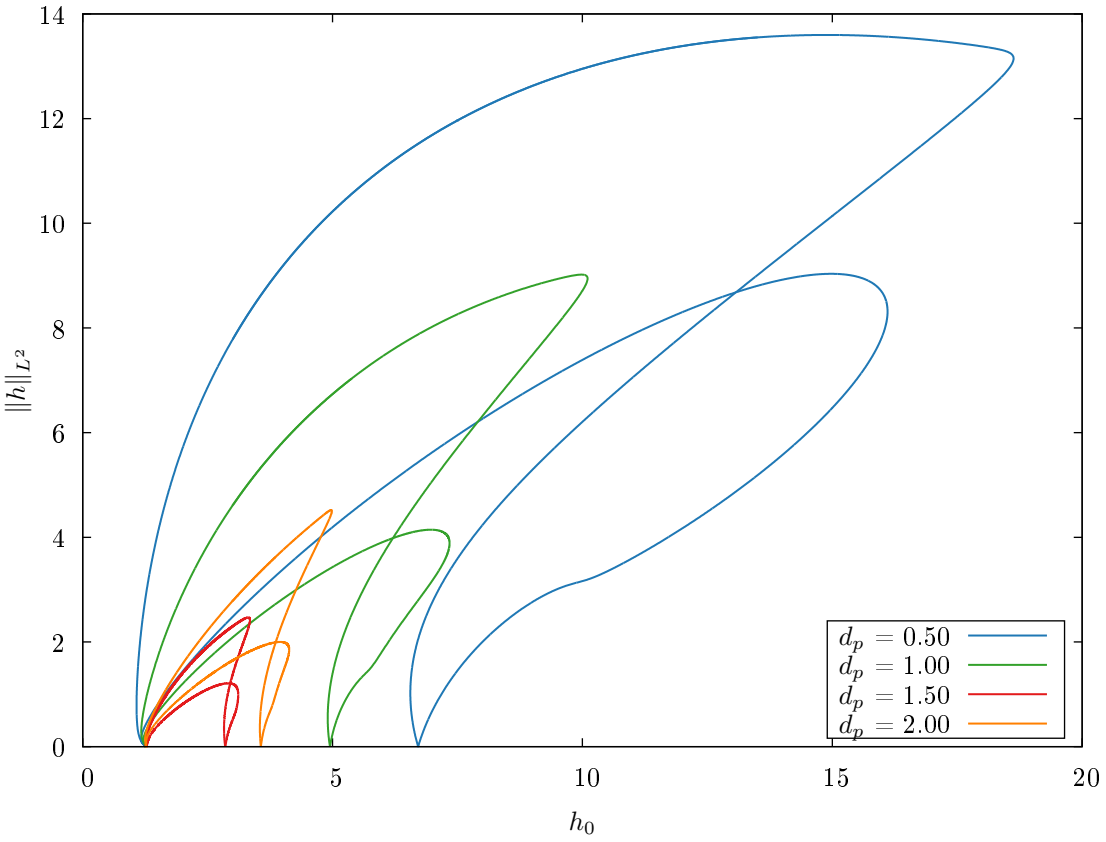

Figure 36: Bifurcation diagram showing the L^2-norm $\|h\|_2$ while varying the mean layer thickness h_0 at different drop numbers d_p. The domain size for this continuation is given by $L = 100$.

The energy plot in the next figure (37) shows a comparison to a cartesian 2D simulation with a mask to restrict the domain to a circle produced by the *Matlab* toolbox pde2path by Sebastian Engelnkemper. As one can see, the curves are identical except for some small deviations when the solution meets the unnatural mask in pde2path.

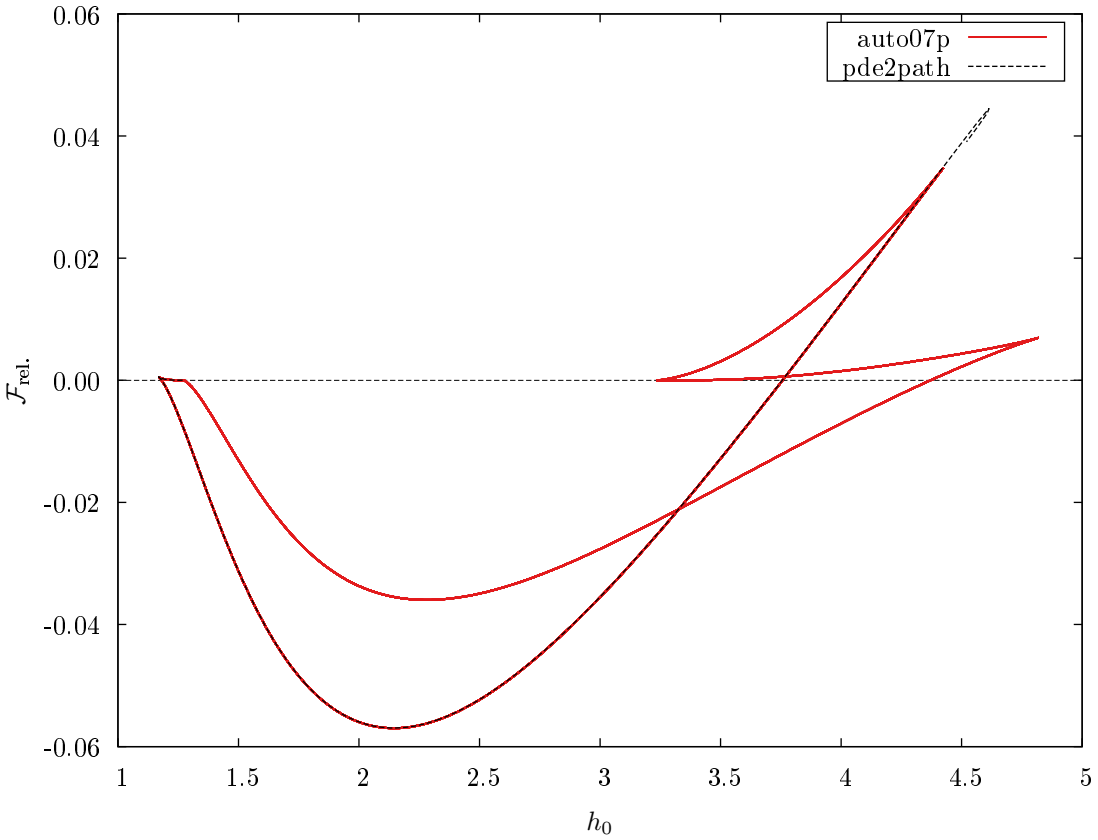

Figure 37: Comparison of the relative free energy curve at a domain size $L = 25$ and a drop number of $d_p = 0.5$ with a curve produced by the *Matlab* toolbox pde2path.

To switch between the branches of the solutions for different drop numbers d_p the derivative at the right boundary is used in a continuation technique. The derivative is increased and decreased periodically to give the system a chance to switch the solution branch which it luckily does. The L^2-norm and the energy during this process are shown in the figure (38).

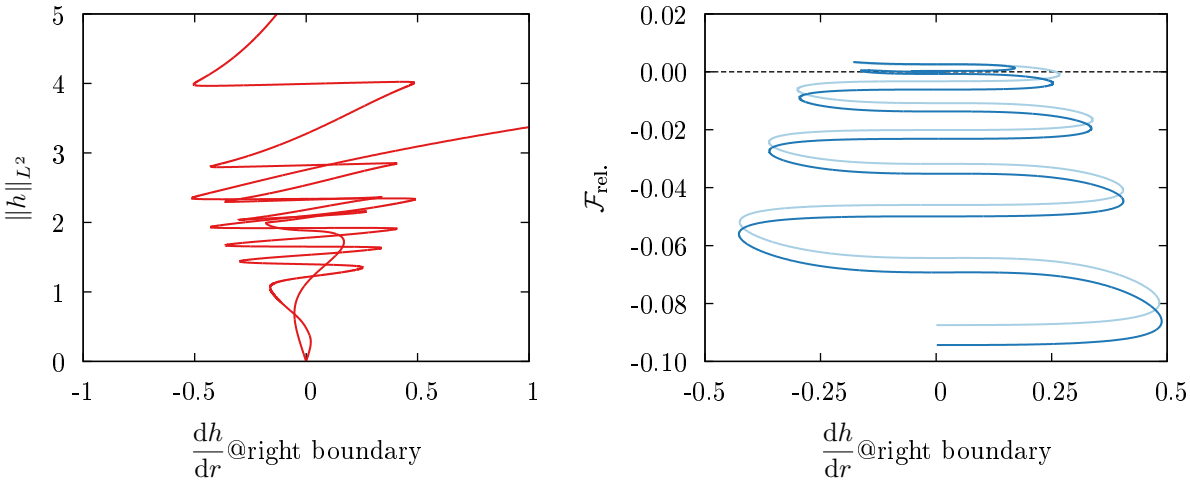

Figure 38: Left: L^2-norm while going through the drop periods at a domain size $L = 150$. Right: Relativ free energy while going through the same drop periods. Light blue: Increasing period. Dark blue: Decreasing period.

The general equation has the structure of a damped harmonic oscillator:

$$\frac{\mathrm{d}^2 h(r)}{\mathrm{d}r^2} + \frac{1}{r}\frac{\mathrm{d}h(r)}{\mathrm{d}r} + g(r) = 0. \tag{2.2}$$

this can also be seen in the phase space as is shown in figure (39).

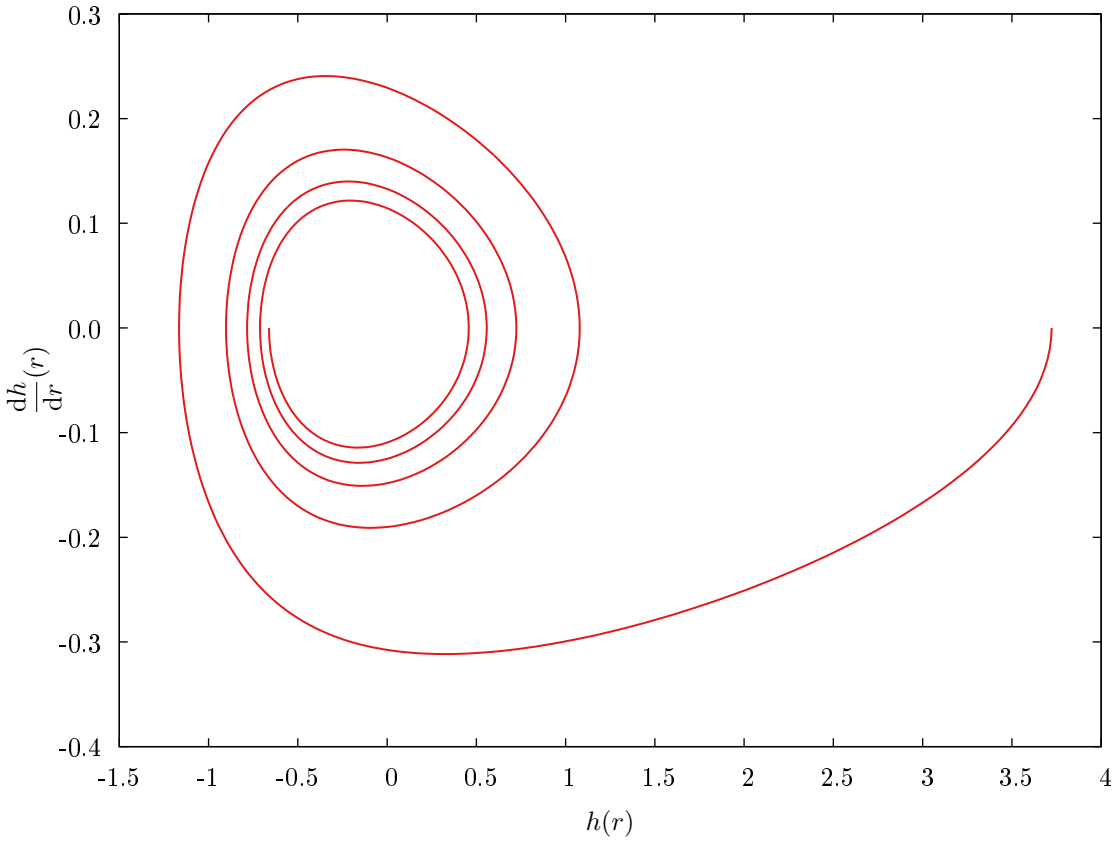

Figure 39: Phasespace of a damped harmonic oscillator created by the equation for the radial thin film model.

B.1 Linear stability

The radial thin film equation is a partial differential equation of the form:

$$\frac{\partial}{\partial t}h(r,t) = \frac{1}{r}\frac{\partial}{\partial r}\left[rQ(h(r,t))\frac{\partial}{\partial r}\left\{-\gamma\left(\frac{\partial^2}{\partial r^2}h(r,t) + \frac{1}{r}\frac{\partial}{\partial r}h(r,t)\right) + \Pi(h)\right]\right\}.$$

The inner bracket has the form of a *Bessel* differential equation:

$$y'' + \frac{1}{x}y' + \left(\frac{x^2 - n^2}{x^2}\right)y = 0.$$

The solution of this equation is given by the *Bessel* function of first kind $J_n(x)$ [47]. In our case, the differential equation has the form of the *Bessel* differential equation with $n = 0$, therefore we have the following ansatz for the linear stability analysis:

$$\tilde{h}(r,t) = h_0 + \epsilon J_0(kr)\mathrm{e}^{\beta t}.$$

In which h_0 is a stable homogenous state that satisfies the thin film equation. To continue the derivation rules for *Bessel* functions are needed which are given by [7]:

$$\frac{\mathrm{d}}{\mathrm{d}r}J_n(r) = \begin{cases} -J_1(r) & \text{, for } n = 0. \\ \frac{1}{2}\left(J_{n-1}(r) - J_{n+1}(r)\right) & \text{, for } n > 0. \end{cases}$$

Substitution this ansatz in the radial thin film equation:

$$\begin{aligned}
\left(\epsilon J_0(kr)\mathrm{e}^{\beta t}\right)\beta &= \frac{1}{r}Q(h_0)\left[-\epsilon\gamma k J_1(kr)\mathrm{e}^{\beta t} + \frac{\partial}{\partial r}\left(\Pi(h_0) + \epsilon J_0(kr)\mathrm{e}^{\beta t}\frac{\partial}{\partial h}\Pi(h)\Big|_{h_0}\right)\right] \\
&\quad + Q(h_0)\left[\frac{\epsilon\gamma k^2}{2}\left(J_2(kr) - J_0(kr)\right)\mathrm{e}^{\beta t} + \frac{\partial^2}{\partial r^2}\left(\Pi(h_0) + \epsilon J_0(kr)\mathrm{e}^{\beta t}\frac{\partial}{\partial h}\Pi(h)\Big|_{h_0}\right)\right] \\
&= \frac{1}{r}Q(h_0)\left[-\epsilon\gamma k J_1(kr)\mathrm{e}^{\beta t} - \epsilon k J_1(kr)\mathrm{e}^{\beta t}\frac{\partial}{\partial h}\Pi(h)\Big|_{h_0}\right] \\
&\quad + Q(h_0)\left[-\frac{\epsilon\gamma k^2}{2}\left(J_0(kr) - J_2(kr)\right)\mathrm{e}^{\beta t} - \frac{\epsilon k^2}{2}\left(J_0(kr) - J_2(kr)\right)\mathrm{e}^{\beta t}\frac{\partial}{\partial h}\Pi(h)\Big|_{h_0}\right] \\
\Leftrightarrow \beta &= \left(\frac{k}{r}\frac{J_1(kr)}{J_0(kr)} + \frac{k^2}{2}\left(1 - \frac{J_2(kr)}{J_0(kr)}\right)\right)\left[Q(h_0)\left(-\gamma - \frac{\partial}{\partial h}\Pi(h)\big|_{h_0}\right)\right] \\
&= k^2 Q(h_0)\left(-\gamma - \frac{\partial}{\partial h}\Pi(h)\big|_{h_0}\right).
\end{aligned}$$

Accordingly, the critical wavenumber k_c is given by:

$$\frac{\partial}{\partial k}\beta(k)\big|_{k=k_c} = 2k_c Q(h_0)\left(-\gamma - \frac{\partial}{\partial h}\Pi(h)\big|_{h_0}\right) \stackrel{!}{=} 0 \Rightarrow k_c = 0. \tag{2.3}$$

If β is smaller zero, the solution is stable and if it is greater than zero it is unstable. Therefore, we restructure the equation for β to:

$$\beta = -k^2 Q(h_0)\left(\gamma + \frac{\partial}{\partial h}\Pi(h)\big|_{h_0}\right). \tag{2.4}$$

Since γ is the always positively defined surface tension it directly follows that the solution is stable if $\frac{\partial}{\partial h}\Pi(h)\big|_{h_0} > -\gamma$ and unstable if $\frac{\partial}{\partial h}\Pi(h)\big|_{h_0} < -\gamma$. Or, if we express the disjoining pressure $\Pi(h)$ as the negative derivative of the interaction potential $\Pi(h) = -\partial_h f(h)$, we get:

$$\text{stable: } \frac{\partial^2}{\partial h^2}f(h)\big|_{h_0} > \gamma, \quad \text{unstable: } \frac{\partial^2}{\partial h^2}f(h)\big|_{h_0} < \gamma. \tag{2.5}$$

C Solution plots

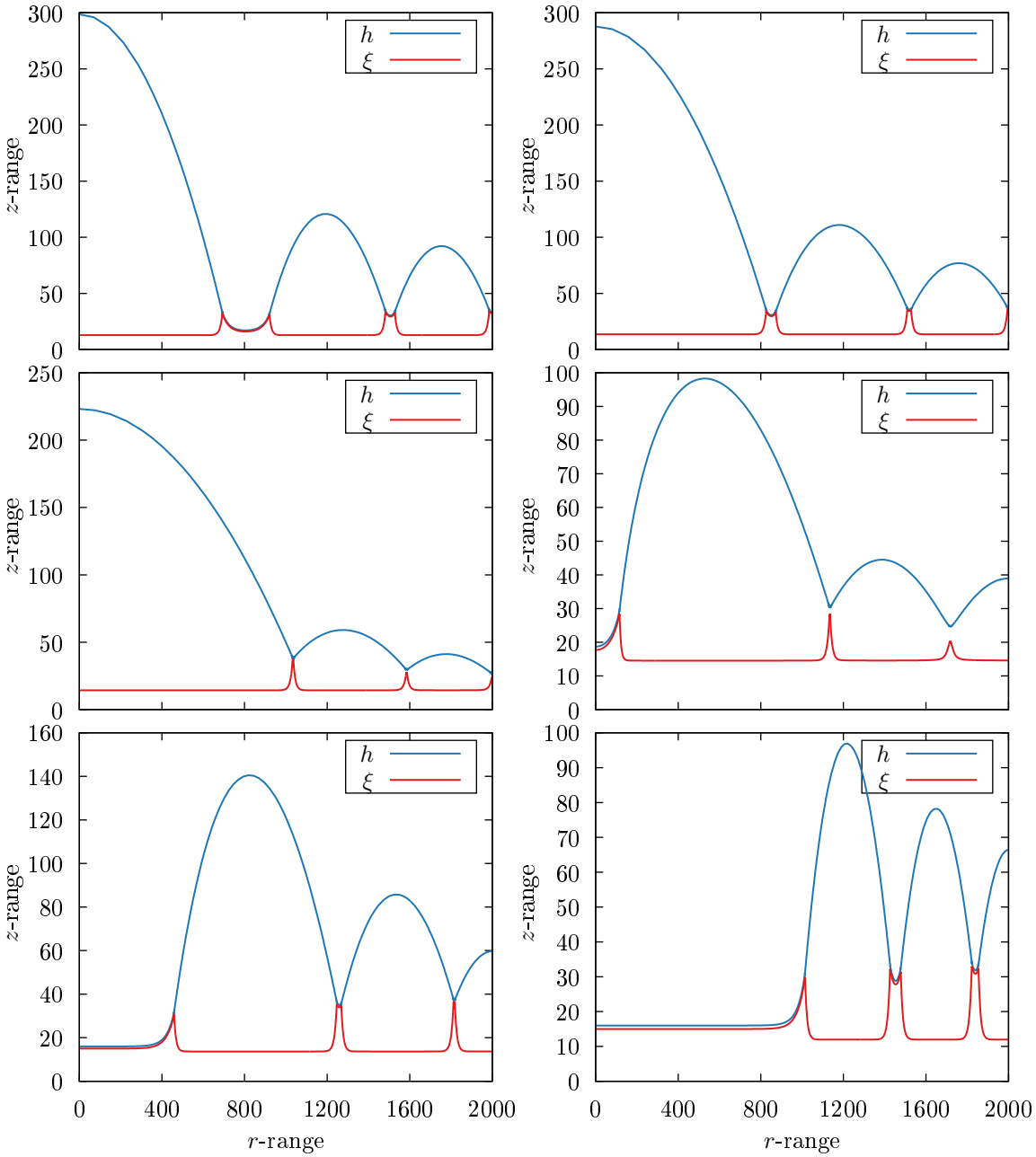

Figure 40: Solutions of the radial elastic model at domain size of L=2000, $\sigma = \frac{\gamma_l}{\gamma_s} = 0.1$, a compression elasticity of $\kappa_v = 0.001$ and a drop number of $d_p = 2.5$.